CHALMERS

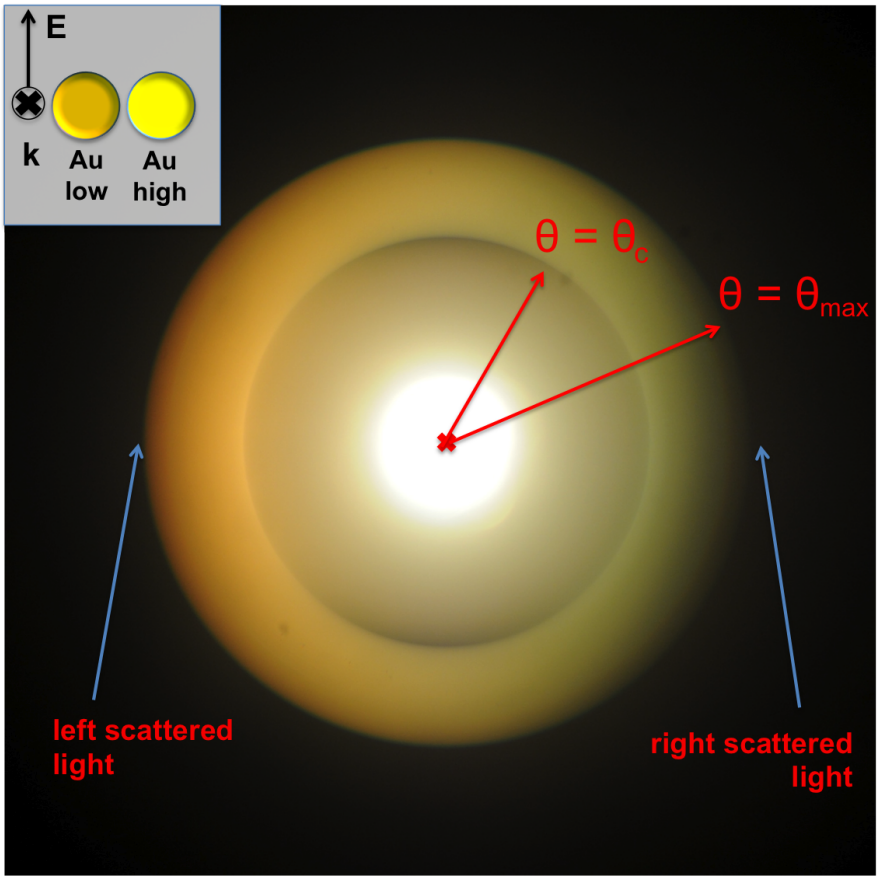

Directional plasmonic nano-sensors

Master's Thesis in Applied Physics

MARTIN WERSÄLL

Bionanophotonics, Applied Physics
Chalmers University of Technology
Göteborg, Sweden 2013
Master's Thesis 2013:1

MASTER'S THESIS

Directional plasmonic nano-sensors

MARTIN WERSÄLL

SUPERVISOR
Assistant Professor Timur Shegai
Chalmers University of Technology

EXAMINER
Professor Mikael Käll
Chalmers University of Technology

Department of Applied Physics
Bionanophotonics
CHALMERS UNIVERSITY OF TECHNOLOGY
Göteborg, Sweden 2013

Directional plasmonic nano-sensors

Master's Thesis within the Applied Physics Masters Programme
MARTIN WERSÄLL

Department of Applied Physics
Bionanophotonics
Chalmers University of Technology
SE-412 96 Göteborg
Sweden
Telephone: +46 (0)31-772 1000

Chalmers Reproservice
Göteborg, Sweden 2013

Abstract

For the last decade plasmonic nanoparticles has been considered as promising candidates for future sensing applications. Due to their incredible ability to detect minute changes in their local dielectric environment, plasmonic nanoparticles exhibit numerous properties suitable for material and biomedical industries.
General methods, which utilizes localized surface plasmon resonances (LSPR) for sensing, are based on detecting extinction resonance peak shift in order to observe changes in refractive index of the local environment. In this study we instead focus on a self-referenced label-free sensing scheme based on directional scattering from samples consisting of asymmetric monometallic Au dimers.
LSPR peak shift measurements moreover often relies on complicated and expensive measuring devices such as microscopes and spectrometers. In order to further suppress economic cost and simultaneously increase simplicity a microscope-free optical setup was designed and manufactured to perform single-wavelength experimental sensing measurements. All samples were manufactured using the hole-mask colloidal lithography method. We also present theoretical models illustrating how supreme sensitivity can be achieved, using a sensing scheme which measures ratio of intensities scattered in opposite directions from asymmetric nanostructures. Moreover experimental bulk- and local refractometric measurements are conducted to support the ability of performing biosensing.

Acknowledgements

During this project there have been several inspiring and helpful people involved to whom I owe sincere gratitude.

To begin with I would like to thank Dr. Ruggero Verre and Robin Ogier for spending a lot of time and effort manufacturing the nanosamples. Thanks to Dr. Andreas Dahlin for software codes and borrowing of experimental device, Jan-Åke Wiman for engineering special components for the optical setup, Gülis Zengin for software skills and rewarding discussions, Mikael Svedendahl for borrowing equipment and nice discussions regarding the project. Thanks to Professor Mikael Käll for general discussions and input on the project aspects.
Finally I would like to dedicate a special amount of gratitude towards my supervisor Dr. Timur Shegai for splendid supervision during the whole project, whom have been a true source of knowledge and inspiration.

Martin Wersäll, Göteborg 5/6 2013

Contents

1

Introduction

Plasmonic nanoparticles is a hot field for present scientific researchers for many different reasons. First and foremost they support the ability to focus light to spatial geometries smaller than the diffraction limit which have built a basis for several new exquisite scientific inventions such as surface-enhanced Raman scattering (SERS) [1].

Even though the research field of plasmonic nanoparticles is relatively young its numerous applications already show great promise for the future in industries such as material science and biomedicine. Due to the extreme sensitivity of plasmons to changes in the dielectric surroundings, which enables them to detect slight shifts in their local environment, they are viewed as highly applicable candidates in different sensing schemes. For example, experiments have been conducted showing that a certain system of plasmonic nanoparticles can act as a highly sensitive hydrogen sensor which is an important aspect due to huge explosive risk of hydrogen gases [2]. This also becomes a very important parameter in future development of fuel cell technologies which is one of the main promising platforms for future sustainable development.
Furthermore it has also been shown that similar types of nanoparticle systems can act as an immensely sensitive biosensor for detection of low concentrations of toxins which stems from cancer cells [3]. By attaching certain receptors to the surface of the nanoparticle one allows certain biomolecules to bind which results in a change of the local dielectric properties in the ambient environment of the nanoparticle. Hence one has the possibility to read out that a certain amount of molecules are found in a specific medium by studying the shift of the local plasmon resonance peak.
Another very important aspect of these nanoplasmonic sensing platforms are that these systems can be constructed in a relatively simple manner. This indicates that they fit very well in to the public demands on cost and convenience.

One of the goals in this project is to further suppress expenses and increase simplicity. Hence this study focuses on an alternative sensing scheme based on angular scattering rather than peak position measurements, motivated by the fact that one can construct sensors working on single-wavelength, that are both spectrometer- and microscope-free. Moreover systems based on this sensing scheme are self-referenced which is another advantageous property compared to many other sensing platforms.
A self-constructed microscope-free optical setup, with the ability to perform biosensing using samples of asymmetric monometallic nanosized Au dimers, was designed and realized during this work. The studied samples consists of Au nanodisks with slightly different heights arranged pairwise as dimers on top of a glass substrate. In this way it is possible to use interference patterns which originates from asymmetric nanoantennas with slightly detuned plasmon resonances, to achieve directional scattering effects.

The beginning of the reports focuses on theories of general plasmonics and scattering of light from nanosized objects, which gradually allows us to simulate and optimize a specific configuration for the nanodimer disks. General information about present plasmonic sensing platforms are furthermore described with emphasized benefits and drawbacks. Finally a new type of sensing platform, using directional scattering, is described and supported with experimental data. Moreover measurements, in the previously mentioned microscope-free optical setup, are presented and demonstrated for both bulk- and local refractometric sensing.

2

Theory of plasmons and optical response of nanoparticles

The response of a metal to an external electromagnetic field can in many cases be described rather well by the dynamics of its conduction electrons. A model that is widely used to simulate the electron dynamics in metals is the Drude-model which states that conduction electrons are "free" and moves as non-interacting particles similar to an electron gas [4].
When studying metal nanoparticles the electron gas is spatially confined to a region much shorter than the wavelength of the incident electromagnetic field. Hence when the incident oscillating field $\mathbf{E}(\mathbf{r}, t)$ reaches the nanoparticle it will displace the electrons with a force corresponding to $\mathbf{F}(\mathbf{r}, t) = -e\mathbf{E}(\mathbf{r}, t)$. A restoring force will arise due to the charge separation between displaced electrons and the positively charged lattice. These forces will in turn give rise to coherent periodic oscillation of electrons called *localized surface plasmons*. These plasmons occur at specific resonance frequencies/wavelengths which highly depends on factors like the geometry of the particle [4].

2.1 Plasmons in noble metals

First of all it is wise to start investigating the optical properties of noble metals by using a classical electrodynamical picture.
According to Maxwell's equations the electric displacement field $\mathbf{D}(\omega)$ in a medium with dielectric function $\epsilon(\omega)$ can be expressed as

$$\mathbf{D}(\omega) = \epsilon_0 \epsilon(\omega) \mathbf{E}(\omega) = \epsilon_0 \mathbf{E}(\omega) + \mathbf{P}(\omega) \tag{2.1}$$

where ϵ_0 is the vacuum permittivity and $\mathbf{P}(\omega)$ is the frequency dependent polarization vector [4].

If one furthermore adopt the so called Drude-Sommerfeld model the equation of motion for a conduction electron may be expressed according to

$$m\frac{\partial^2 \mathbf{r}}{\partial t^2} + m\gamma\frac{\partial \mathbf{r}}{\partial t} = -e\mathbf{E}(t) \tag{2.2}$$

where γ is a damping parameter, e the magnitude of the electron charge and m the free electron mass.
Via a Fourier transformation in the time domain, the solution for $\mathbf{r}$ in frequency space is given by

$$\mathbf{r}(\omega) = \frac{e/m}{\omega^2 + i\gamma\omega}\mathbf{E}(\omega) \tag{2.3}$$

where i denotes the imaginary unit [5]. Since the polarization vector is described by the amount of dipole moments per unit volume, it is now convenient to express the polarization as $\mathbf{P}(\omega)$ = -n$_e$e$\mathbf{r}(\omega)$, where n_e is the density of electrons.
By combining equations (2.1) and (2.3) the dielectric function for the free electrons can be written as

$$\epsilon_f(\omega) = 1 - \frac{\omega_p^2}{\omega^2 + i\gamma\omega} \tag{2.4}$$

where $\omega_p = \sqrt{\frac{n_e e^2}{\epsilon_0 m}}$ is the plasma frequency.

The previously described model works quite well for simulating the optical properties of gold in the near infrared regime. However, for incident light with higher energies ($E > 2.26$ eV $\Leftrightarrow \lambda < 550$ nm) one have to take into account that excitations of electrons from lower lying bands into the conduction band might occur [4]. Due to this phenomena the equation of motion in equation (2.2) have to be redefined to include a force term from the nuclei potential according to $\beta\mathbf{r}$, which results in a expression for the interband dielectric function $\epsilon_{ib}(\omega)$ as

$$\epsilon_{ib}(\omega) = 1 - \frac{\tilde{\omega}_p^2}{(\omega^2 - \omega_0^2) + i\Gamma\omega} \tag{2.5}$$

where $\omega_0 = \sqrt{\beta/m^*}$, Γ the damping factor for bound electrons, $\tilde{\omega}_p = \sqrt{\frac{\tilde{n}_e e^2}{\epsilon_0 m^*}}$ where $\tilde{n}_e$ describes the density of bound electrons and m^* is their effective mass.

However in this study the phenomena to be investigated are aimed to occur at wavelengths higher than 550 nm, which means that the expression in equation (2.4) is still a valid approximation in our case.
The real part of the dielectric function is related to stored energy within the medium and the imaginary part to energy dissipation [4]. These parts can be viewed in Figure 2.1 where it is obvious that the real/imaginary part of the dielectric function is negative/positive for all wavelengths in the considered spectral region. This is in agreement that light can only penetrate a metal to a very small extent, since if the real part of the

dielectric function ϵ_r is negative the imaginary part of the refractive index n_i becomes strong ($n = \sqrt{\epsilon_f}$). From this knowledge and the relation $k = k_0 n = k_0(n_r + in_i) \Rightarrow \mathbf{E} = \mathbf{E}_0 e^{i(k_0 nR - \omega t)} = \mathbf{E}_0 e^{-k_0 n_i R} e^{i(k_0 n_r R - \omega t)}$ where R describes the spatial coordinate traveled by the wave, it is obvious that the imaginary part of the refractive index is responsible for the decay of the electric field within a certain medium.

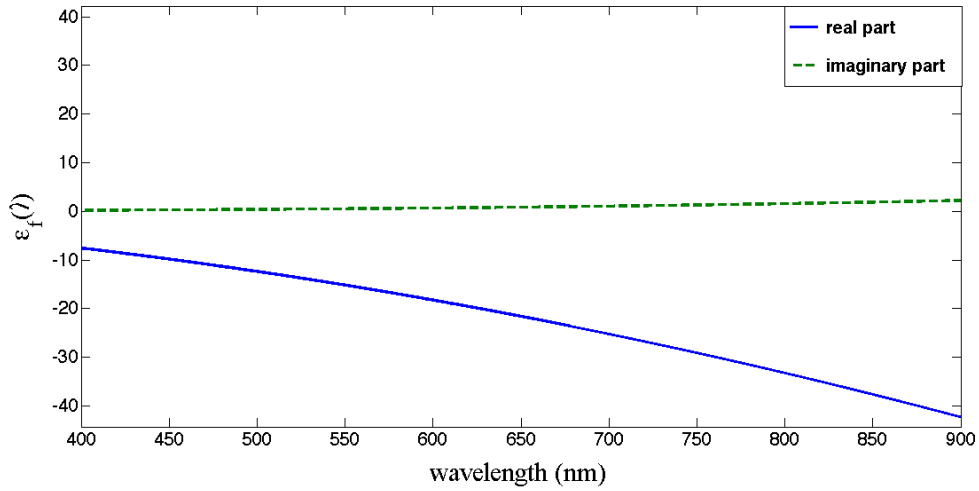

Figure 2.1: *The dependence between dielectric function for gold and wavelength of incident light. Notice that the real part of the dielectric function has negative value for all wavelengths in the studied spectral region which shows that light can only penetrate gold to a small extent.*

2.2 Plasmonic nanoparticles

In the quasi-static (Rayleigh) approximation, the polarizability $\alpha(\omega)$ for a spherical nanoparticle with spatial dimensions much smaller than the wavelength of the incident light, can be expressed via the Clausius-Mossotti relation

$$\alpha(\omega) = 4\pi R^3 \frac{\epsilon(\omega) - \epsilon_d}{\epsilon(\omega) + 2\epsilon_d} \tag{2.6}$$

where R is the radius of the spherical nanoparticle and ϵ_d is the dielectric function of the surrounding environment [6].
By assuming that the dielectric function of the surrounding medium is constant over the whole visible spectra one discovers that it is possible to find a frequency which maximizes the polarizability function. This maximum occurs for a frequency ω_0 which results that the condition $\mathrm{Re}\{\epsilon(\omega)\} + 2\epsilon_d = 0$ is fulfilled, i.e. the real part of the denominator in equation (2.6) becomes zero.
Since the relation between polarizability function and dipole moment is $\mathbf{p}(\omega) = \epsilon_d \alpha(\omega)\mathbf{E}(\omega)$ we see that a maximum in dipole moment occurs for the same frequency ω_0 as well.

This effect results in a very high probability for the incident light to excite dipoles and is a phenomena called *localized surface plasmon resonance (LSPR)*, which stems from coherent oscillations of spatially confined conduction electrons in the nanosized particle. Since different metals are described with different dielectric functions two geometrically equal nanoparticles made of different materials will still yield a different LSPR. It turns out that the plasmon resonance is also highly dependent on the geometric shape of the specific nanoparticle which is described in the following section.

2.3 Light scattering from nanosized spheroids

The previously described polarizability function in equation (2.6) is only valid for spherical nanoparticles. For other geometries such as disk shaped nanoparticles one cannot really state that this polarizability function is suitable for describing the optical response to an external electric field.
However, the disk shaped particles may be approximated as oblate spheroids ($a = b > c$) with semi axes $r_x = a$, $r_y = b$ $(= a)$ and $r_z = c$, and with low aspect ratios[1]. By doing this equation (2.6) may be adjusted with a *geometrical form factor* L_n, which stems from solving Laplace's equation in ellipsoidal coordinates, according to

$$L_n = \frac{abc}{2} \int_0^\infty \frac{1}{(s + r_n^2)\sqrt{(s + a^2)(s + b^2)(s + c^2)}} \, \mathrm{d}s \tag{2.7}$$

where $n \in \{x, y, z\}$. Furthermore for oblate spheroids we could analytically express L_x according to

$$L_x = \frac{\sqrt{1 - e^2}}{2e^3} \left(\frac{\pi}{2} - \arctan \left[\sqrt{\frac{1 - e^2}{e^2}} \right] \right) - \frac{1 - e^2}{2e^2} \tag{2.8}$$

where $e = \sqrt{1 - \frac{c^2}{a^2}}$. Hence the geometrical form factor for a nearly disk shaped object depends exclusively on aspect ratio [6].
This results in an expression for the polarizability function along an arbitrary axis (x, y or z) as

$$\alpha_n(\omega) = V \frac{\epsilon(\omega) - \epsilon_d}{\epsilon_d + L_n[\epsilon(\omega) - \epsilon_d]} \tag{2.9}$$

where $V = \frac{4}{3}\pi abc$ is the volume of the spheroid.
By inserting the relation for the dielectric function, described in equation (2.4), into (2.9) it can be shown that the resonance occurs at a frequency

$$\omega_{LSPR} = \frac{\omega_p}{\sqrt{1 + (1/L_n - 1)\epsilon_d}} \tag{2.10}$$

This expression certainly states that a shift will occur in the LSPR when the refractive index n_d changes since the relation between the dielectric function and refractive index

[1] the ratio of the vertical- and horizontal semi axis of a spheroid, $\tilde{R} = \frac{c}{a}$.

is $\epsilon_d = n_d^2$. This is one of the most essential aspects in plasmonic sensing [1].
The expression for the polarizability function, in equation (2.9), does not account for factors like radiation-damping or dynamic depolarization which must be paid attention to in order to get a more accurate estimation of both the spectral position ω_{LSPR} and the overall shape of the resonance peak.
However this expression gives a rough understanding of the shift in LSPR wavelength due to geometrical parameters like diameter and height. This is illustrated in Figure 2.2 which is based on equations (2.8) and (2.10) with parameters $\omega_p = 13.08{\cdot}10^{15}\ s^{-1}$, $\gamma = 1.075{\cdot}10^{14}\ s^{-1}$ which are reasonable values for Au [10]. All curves are plotted using the same refractive index $n_d = 1.0$.
From this illustration it is clear to state that the local surface plasmon resonance of the nanoparticle redshifts/blueshifts[2] with increasing diameter/height respectively. Moreover it is clear that each resonance peak have a Lorentzian shaped feature, which corresponds to damped oscillatory dynamics in the time domain [11]. An additional important factor to take into account when investigating scattered light from nanosized objects is that scattering heavily depends on the volume of the particle. In the electrostatic approximation it is shown that the scattering cross section σ_{sca} can be expressed as

$$\sigma_{sca}(\omega) = \frac{k^4}{6\pi}|\alpha(\omega)|^2 \tag{2.11}$$

where the relation to amount of scattered intensity is $I_{sca} = \frac{I_0(\omega)}{A}\sigma_{sca}(\omega)$. Here A describes the geometrical cross section of the nanoparticle and $I_0(\omega)$ the intensity of the incident light. Moreover the extinction cross section is expressed as

$$\sigma_{ext}(\omega) = kIm\{\alpha(\omega)\} \tag{2.12}$$

and hence the expression for absorption cross section is $\sigma_{abs}(\omega) = \sigma_{ext}(\omega) - \sigma_{sca}(\omega)$.
Since the polarizability function $\alpha(\omega)$ depends linearly on the volume (see equation 2.9) the scattered intensity will have a quadratic dependence on the volume of the nanoparticle. This knowledge is of great importance when conducting experimental studies, since it is almost impossible to measure scattered light from too small particles due to factors like noise levels.

2.4 Radiation of dipoles located near planar interfaces

As stated earlier the polarizability function $\alpha_n(\omega)$ in equation (2.9) reaches a maximum value when the wavelength of the incident light corresponds to that of λ_{LSPR} for the nanodisk. This means that the particle will radiate a lot of light in directions both left and right perpendicular to the axis along which the charge density oscillates [14].

An interesting aspect of scattering from nanosized objects takes place when considering oscillating dipoles located near a plane surface. A unique radiation pattern arises due

[2] redshift/blueshift corresponds to an increase/decrease in wavelength.

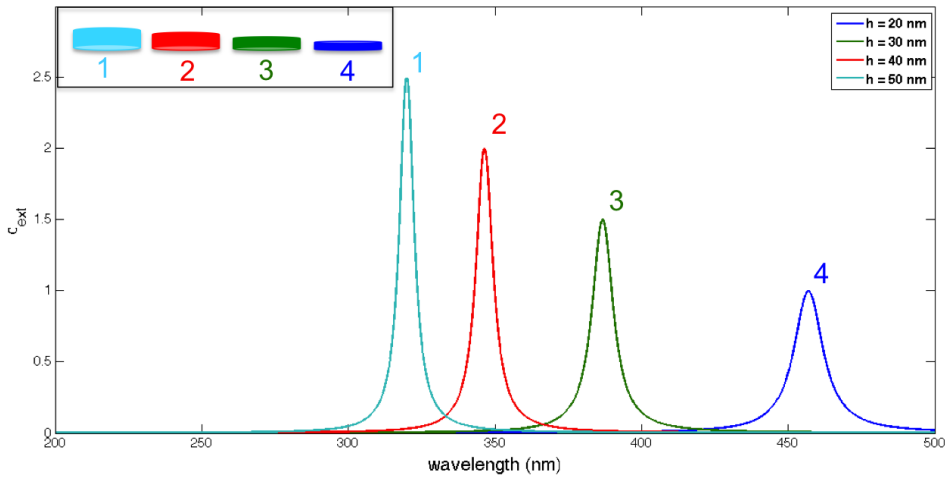

(a) *Illustration of how the extinction spectrum varies with aspect ratio of a nanodisk. In this case the diameter $D = 150$ nm are the same in every disk. The inset figure illustrates which geometric dimensions corresponds to which resonance peak.*

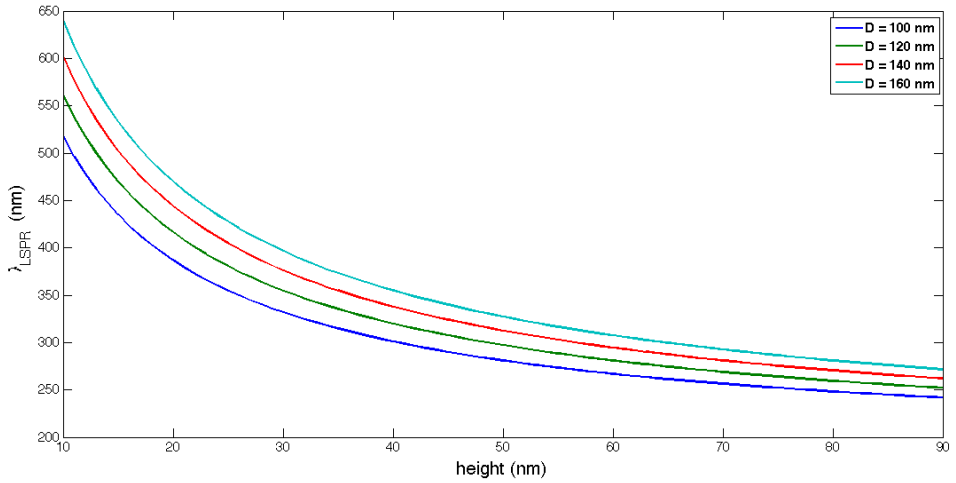

(b) *A general overview of how the local surface plasmon resonance wavelength λ_{LSPR} changes with aspect ratio of the disk.*

Figure 2.2: *Illustration of how the local plasmon resonance varies when the aspect ratio of the disk changes.*

to properties of evanescent fields. The explicit expression for the radiation pattern can be derived by the following steps.
We start by writing the time averaged Poynting vector as $\langle \mathbf{S} \rangle = \frac{1}{2}\mathrm{Re}\{\mathbf{E} \times \mathbf{H}^*\}$. By then using the fact that the relation between electric and magnetic field in the far-zone is $\hat{\mathbf{n}}_k \times \mathbf{E} = v\mathbf{B} \Rightarrow \mathbf{H} = v^{-1}\mu^{-1}\hat{\mathbf{n}}_k \times \mathbf{E}$ ($v = \frac{\omega}{k}$), it is straight forward to show that the far-field expression of the time-averaged Poynting vector $\langle \mathbf{S} \rangle_{far}$ is

$$\langle \mathbf{S} \rangle_{far} = \frac{1}{2}\sqrt{\frac{\epsilon_0 \epsilon_j}{\mu_0 \mu_j}}(\mathbf{E} \cdot \mathbf{E}^*)\hat{\mathbf{n}}_k \tag{2.13}$$

where $\hat{\mathbf{n}}_k = \frac{\mathbf{k}}{|\mathbf{k}|}$ is simply a unit vector in the radial direction away from the dipole. Parameters ϵ_j and μ_j are just the dielectric function and magnetic permeability of a certain medium.
Furthermore it is known that the magnitude of the Poynting vector describes the radiated power per unit area crossing a surface with a normal vector parallel to $\mathbf{S}$. Hence the radiated power P per unit solid angle can be expressed according to

$$P = p(\Omega)d\Omega = r^2 \langle \mathbf{S} \rangle_{far} \cdot \hat{\mathbf{n}}_k \tag{2.14}$$

By assigning the dipole moment $\boldsymbol{\mu} = (\mu_x, \mu_y, \mu_z)$ to the oscillating charge density of the nanodisk the far-field may be represented according to

$$\mathbf{E} = \begin{bmatrix} E_\theta \\ E_\phi \end{bmatrix} = \frac{k_1^2}{4\pi\epsilon_0\epsilon_1}\frac{e^{ik_2 r}}{r}\begin{bmatrix} [\mu_x \cos\phi + \mu_y \sin\phi]\cos\theta \boldsymbol{\Phi}_2^{(2)} - \mu_z \sin\theta \boldsymbol{\Phi}_2^{(1)} \\ -[\mu_x \sin\phi - \mu_y \cos\phi]\boldsymbol{\Phi}_2^{(3)} \end{bmatrix} \tag{2.15}$$

Thus from equations (2.13), (2.14) and (2.15) it is now possible to deduce the normalized radiation pattern, in the medium below the plane surface, as

$$\begin{aligned} \frac{p\,(\theta,\phi)}{P_0} = \frac{3\epsilon_2 n_1}{8\pi\epsilon_1 n_2 |\boldsymbol{\mu}|^2}\Big[& \mu_z^2 \sin^2\theta |\boldsymbol{\Phi}_2^{(1)}|^2 + [\mu_x\cos\phi + \mu_y \sin\phi]^2 \cos^2\theta |\boldsymbol{\Phi}_2^{(2)}|^2 \\ & + [\mu_x \sin\phi - \mu_y \cos\phi]^2 |\boldsymbol{\Phi}_2^{(3)}|^2 - \mu_z[\mu_x \cos\phi \\ & + \mu_y \sin\phi]\cos\theta \sin\theta \big[\boldsymbol{\Phi}_2^{*(1)}\boldsymbol{\Phi}_2^{(2)} + \boldsymbol{\Phi}_2^{(1)}\boldsymbol{\Phi}_2^{*(2)}\big]\Big] \end{aligned} \tag{2.16}$$

where P_0 corresponds to the total amount of energy dissipation in a homogeneous medium characterized by ϵ_1 and μ_1. The parameters $\boldsymbol{\Phi}_2^{(1)}$, $\boldsymbol{\Phi}_2^{(2)}$ and $\boldsymbol{\Phi}_2^{(3)}$ can further be expressed as

$$\boldsymbol{\Phi}_2^{(1)} = \frac{n_2 \cos\theta}{n_1\sqrt{(n_1/n_2)^2 - \sin^2\theta}} t_p(\theta) e^{ik_2[h\sqrt{(n_1/n_2)^2 - \sin^2\theta} + \delta\cos\theta]} \tag{2.17}$$

$$\boldsymbol{\Phi}_2^{(2)} = -\frac{n_2}{n_1} t_p(\theta) e^{ik_2[h\sqrt{(n_1/n_2)^2 - \sin^2\theta} + \delta\cos\theta]} \tag{2.18}$$

$$\boldsymbol{\Phi}_2^{(3)} = \frac{\cos\theta}{\sqrt{(n_1/n_2)^2 - \sin^2\theta}} t_s(\theta) e^{ik_2[h\sqrt{(n_1/n_2)^2 - \sin^2\theta} + \delta\cos\theta]} \tag{2.19}$$

where h describes the height of the dipole over the plane surface and δ the total height of the layered interface. Note that in the case of a single interface, $\delta = 0$. The functions $t_p(\theta)$ and $t_s(\theta)$ are just Fresnel amplitude coefficients for p- and s-polarized components respectively [4].
By studying the angular dependence of the function, described in equation (2.16), one finds that if the dipole is placed closely enough ($\lambda/100 \leq h \leq \lambda/10$) to the plane surface, a significant portion of the radiation pattern will be concentrated in the so called *forbidden zone*. The nature of the fields originating from the radiating dipoles located close above the interface are evanescent but may be transformed into propagating modes below the interface due to refractive index mismatch. The direction for this transformed propagating wave always occur at an angle equal or greater than the critical angle $\theta_c = \arcsin(n_1/n_2)$ with respect to the normal to the lower-upper medium interface. Hence this light can be viewed as *forbidden* in ordinary terms of scattering due to the fact that evanescent fields from dipoles located further away from the plane interface will decay before it ever reaches the interface. Therefore the scattered light from these dipoles will end up in the *allowed zone* of the lower medium. The radiation pattern from dipoles located a distance h above a plane interface is illustrated in Figure 2.3 where the region above/below the dotted lines, in the lower medium, corresponds to the forbidden/allowed zone respectively. Notice that the amount of light scattered into the forbidden zone decreases immensely when the height of the dipole location over the plane interface h increases, whereas the amount of light scattered into the allowed zone is independent of h.

2.5 Coupled dipole- and modified long wavelength approximations

So far we have only described the theory for the interaction between light and a single plasmonic nanoparticle. Since this study involves scattering from asymmetric monometallic dimers it is crucial to investigate what coupling effects that might occur between juxtaposed nanospheroids.
In the case of two interacting plasmonic particles, Miljković *et al.* showed that using *modified long wavelength approximation* (MLWA), which includes corrections for both radiation-damping and dynamic depolarization, more reliable results are obtained when investigating extinction-, scattering- and absorption cross sections [12].
With this model in hand, the polarizability function of a nanosized spheroid can be expressed as

$$\tilde{\alpha}_n(\omega) = \frac{\alpha_n(\omega)}{4\pi - \frac{k^2}{r_n}\alpha_n(\omega) - i\frac{2}{3}k^3\alpha_n(\omega)} \tag{2.20}$$

where $\alpha_n(\omega)$ is referring to the polarizability expression in equation (2.9). The second term in the denominator accounts for the appearance of an enhancement maximum at finite small volumes, and the third term accounts for radiation damping which results in radiation losses and therefore broadens and decreases the magnitude of the resonance

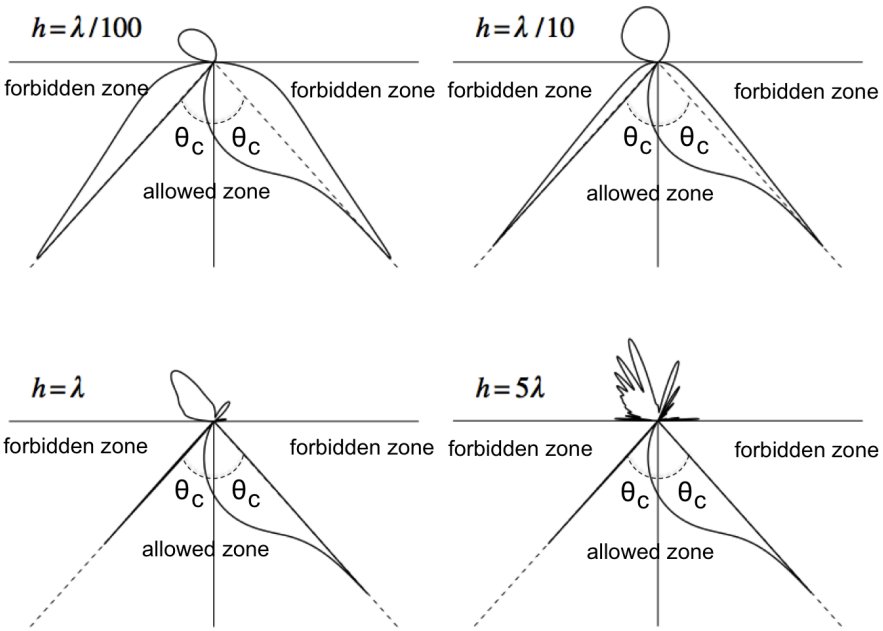

Figure 2.3: *Radiation pattern of a dipole located close to a plane surface, for four different heights h. Note that the radiation pattern in the allowed region of the lower medium is independent of the height which the dipole is place above the surface. θ_c denotes the critical angle of the substrate/upper medium interface. Picture taken from [4].*

peak for larger nanoparticles [13].

Moreover the dipole moment $\mathbf{p}_n$ of a nanoparticle located in a system consisting of several interacting dipoles may be approximated as a point dipole, coupling to surrounding point dipoles. This method is generally referred to as a *coupled dipole approximation* (CDA) where the dipole of a certain nanoparticle may be explicitly expressed as

$$\mathbf{p}_n = \tilde{\alpha}_n(\mathbf{E}_{inc,n} - \sum_{m \neq n} \mathbf{A}_{nm}\mathbf{p}_m) \tag{2.21}$$

where $\mathbf{E}_{inc,n} = \mathbf{E}_0 e^{i(\mathbf{k}\cdot\mathbf{R}_n - \omega t)}$ describes the incident field at position $\mathbf{R}_n$. A further convenient trick is to define $\mathbf{A}_{nn} = \tilde{\alpha}_n^{-1}$, which reduces equation (2.21) to just solving

$$\sum_{m=1}^{2} \mathbf{A}_{nm}\mathbf{p}_m = \mathbf{E}_{inc,n} \tag{2.22}$$

since a dimer system is considered and interaction between two different dipoles needs to be investigated. The dipole interaction term $\mathbf{A}_{12}$ is further explicitly expressed as

$$\mathbf{A}_{12} = \frac{e^{ikR_{12}}}{R_{12}}\left(k^2[\hat{n}_{12}\hat{n}_{12}^T - \mathbf{1}] + \frac{ikR_{12} - 1}{R_{12}^2}[3\hat{n}_{12}\hat{n}_{12}^T - \mathbf{1}]\right) \tag{2.23}$$

where $R_{12} = |\mathbf{R}_2 - \mathbf{R}_1|$, $\hat{n}_{12} = (\mathbf{R}_2 - \mathbf{R}_1)/|\mathbf{R}_2 - \mathbf{R}_1|$ and $\mathbf{1}$ is a 3×3 identity matrix.

By solving equation (2.22) a complex valued expression of the dipole moment $\mathbf{p}_n$ is acquired. In order to get the magnitude and intrinsic phase of the dipole, $|\mathbf{p}_n| = \sqrt{(Re\{\mathbf{p}_n\})^2 + (Im\{\mathbf{p}_n\})^2}$ and $\varphi_n = \arctan\left[\frac{Im\{\mathbf{p}_n\}}{Re\{\mathbf{p}_n\}}\right]$ are calculated respectively.

2.6 Asymmetric monometallic dimers for directional scattering

When the wavelength of the incident light corresponds to the LSPR wavelength of the nano disks the absorption- and scattering cross sections will reach maximum values.
Due to the chosen geometries of the disks, in this study, the LSPR wavelength of the particles will be located in the visible region of the spectrum which means that the nanodisks will radiate light with a wavelength corresponding to their LSPR [14].
If the nanoparticles are ordered in a symmetric structure, for example as separated single disks on a glass substrate all with equal dimensions, the resulting radiation pattern will have an angular scattering symmetry.

If one on the other hand want to create a directional radiation pattern the symmetry of the nanostructures has to be reduced [15]. By replacing each position, where a single nanodisk is located, with a dimer pair consisting of two nanodisks with equal diameter but with different height, the symmetry of the sample is highly subdued. The sizes of the nanoparticles in the asymmetric dimers are much smaller than the wavelength of the radiating light. Hence, from basic knowledge about Huygens's principle the scattered light from each dimer pair can be approximated as originating from two different point sources, since the LSPR of each particle are detuned from each other [16].
To understand how the scattering directionality arises, conditions for interference between the scattered light originating from two different point sources needs to be investigated.

From phasor addition in the complex plane and/or calculating the time average (over a time period T) of the square of the electric field, the total intensity from the scattering dimer at a distance R can be expressed as

$$I = \langle \mathbf{E}^2 \rangle_T \approx \frac{1}{16\pi^2\epsilon_0^2 R^6}\left[|\mathbf{p}_1|^2 + |\mathbf{p}_2|^2 + 2|\mathbf{p}_1||\mathbf{p}_2|\cos\left(kL - \Delta\varphi_{12}\right)\right] \tag{2.24}$$

where $|\mathbf{p}_1|$, $|\mathbf{p}_2|$ and $\Delta\varphi_{12}$ are magnitudes and intrinsic phase difference of the dipoles respectively, $k = \frac{2\pi n}{\lambda}$ where n is refractive index and L the intermediate distance between the dipoles [14], [16]. The last term in expression (2.24) describes the interference between the light originating from the two different radiating sources.

So considering a system consisting of asymmetric monometallic Au dimers located on top

of a plane surface, the ratio of intensities scattered to the left/right along the direction of the dimer axis is expressed according to

$$R_I = \frac{|\mathbf{p}_1|^2 + |\mathbf{p}_2|^2 + 2|\mathbf{p}_1||\mathbf{p}_2|\cos(kL - \Delta\varphi_{12})}{|\mathbf{p}_1|^2 + |\mathbf{p}_2|^2 + 2|\mathbf{p}_1||\mathbf{p}_2|\cos(-kL - \Delta\varphi_{12})} = \frac{1 + f(A)cos(kL - \Delta\varphi_{12})}{1 + f(A)cos(kL + \Delta\varphi_{12})} \quad (2.25)$$

where $A \equiv |\mathbf{p}_1|/|\mathbf{p}_2|$ and $f(A) \equiv \frac{2A}{1+A^2}$. Notice that wavenumbers k and $-k$ corresponds to waves traveling in opposite directions along the dimer axis.
Since both $|\mathbf{p}_1|$, $|\mathbf{p}_2|$ and arguments $\pm kL - \Delta\varphi_{12}$ depends on wavelength λ, it is possible to find a wavelength λ_0 where the ratio in equation (2.25) is maximized. The optimal situation corresponds to a wavelength where $f(A) = 1$ ($|\mathbf{p}_1| = |\mathbf{p}_2|$), $kL + \Delta\varphi_{12} = \pm(\pi + 2\pi m)$ and $kL - \Delta\varphi_{12} = \pm 2\pi m$ (m is an integer number).
It is clear that this condition is fulfilled when $\lambda_0 = 4nL$ and $\Delta\varphi_{12} = \pi/2$ simultaneously. This situation is illustrated in Figure 2.4 which is a simulation of two dipoles, with $|\mathbf{p}_1| = |\mathbf{p}_2|$, placed $L = \lambda/4n$ from each other. Notice how the intensity of the light scattered to the right along the dimer axis vanishes due to destructive interference, as the intrinsic phase difference changes from 0 to $\pi/2$. It can easily be shown that the maximum value for the ratio is highly dependent on a dimer system which fulfills all the conditions, described above, at a certain wavelength λ_0.
Once a highly directional dimer system is engineered, small changes in the surrounding medium will break the previously described "perfect" constructive/destructive interference conditions and hence would lead to dramatic changes in ratio of left/right-scattered intensities. This property is highly suitable for sensing purposes where the main goal is to detect extremely small changes in the ambient dielectric environment.
For instance, if the ratio of dipole magnitudes $\frac{|\mathbf{p}_1(\lambda_0)|}{|\mathbf{p}_2(\lambda_0)|} = 1 \pm 10^{-3}$ simultaneously as $\Delta\varphi_{12}(\lambda_0) = \pi/2$ the maximum value of the intensity ratio will be orders of magnitude lower than in the case where the ratio of the dipole magnitudes would have been equal to one.

An additional parameter to take in consideration, when dealing with interference between different sources, is the *coherence length* L_c. The interpretation of this quantity is briefly the extent in space over which the phase of an electromagnetic wave can be predicted reliably. Hence if the radiating sources are located within a distance smaller than L_c it can be assumed that they are hit by a plane wave, even with a white light source. If these disks instead were located a distance $L \geq L_c$ the interference would be blurred out [16].

It is off course a difficult task tuning a system to fulfill exactly the requirements described above, but it clearly shows that the ratio is highly sensitive to extremely small changes of the system. This is a very much preferable property in this study since the main goal of this system is to work as a biosensor with the ability to detect very small changes in the local dielectric environment. A description of the sensing ability for a directional scattering sample are presented in Chapter 3.3.

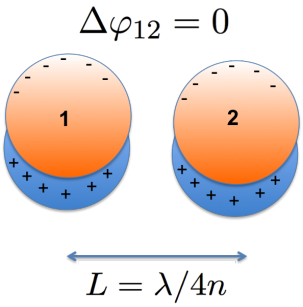

(a) *Illustration of intermediate distance and intrinsic phase difference $\Delta\varphi_{12} = 0$ between two different dipoles.*

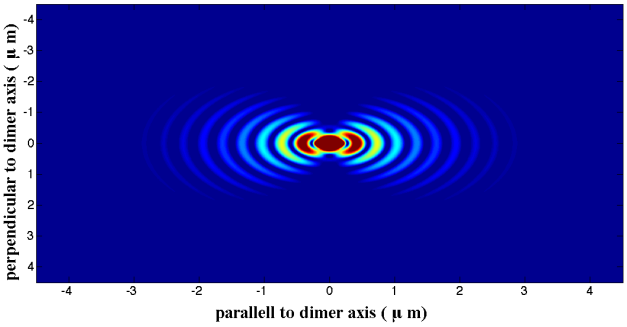

(b) *Simulation of radiation pattern for the dipole configuration illustrated to the left. Since the interference between the two dipole sources are more or less constructive both to left and right along the dimer axis, the radiation pattern appears to be rather symmetric.*

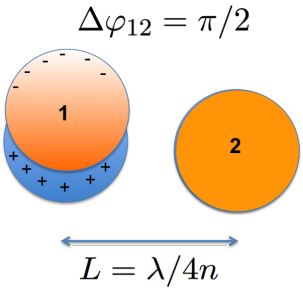

(c) *Illustration of intermediate distance and intrinsic phase difference $\Delta\varphi_{12} = \pi/2$ between two different dipoles.*

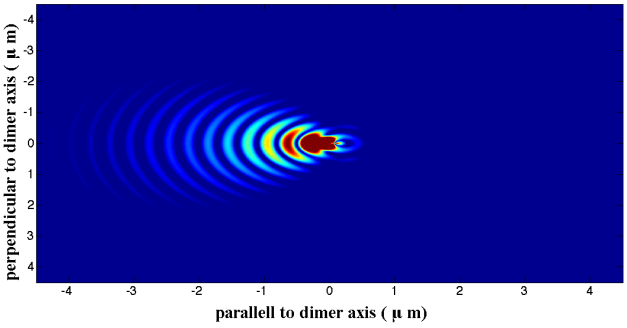

(d) *Simulation of radiation pattern for the dipole configuration illustrated to the left. In this case the interference between the dipoles are constructive in one direction and destructive in the opposite direction along the dimer axis, i.e. directional scattering occurs.*

Figure 2.4: *Illustration of the interference between the radiation from two dipoles with a certain intermediate distance and intrinsic phase difference.*

2.7 Simulation of scattering and absorption cross sections for asymmetric monometallic Au dimers

From the different theoretical models, presented in earlier sections, simulations were carried out in order to find a dimer configuration which geometric dimensions results in the sought properties, i.e. a highly directional scattering system.

The simulations are based on placing two separate spheroids, with dimensions $a_1 = b_1 = 50$ nm, $c_1 = 20$ nm, $a_2 = b_2 = 55$ nm, $c_2 = 15$ nm, along the y-axis with an intermediate center-to-center distance of $L = 135$ nm.
Since the dipoles are located over a substrate we have to distinguish between the upper medium with refractive index n_{top} and the refractive index of the lower medium n_g. In order to simulate the effective refractive index n_{eff} which the nanospheroids experiences, a mean value of the dielectric functions for the upper and lower medium was taken resulting in $n_{eff} = \sqrt{(n_{top}^2 + n_g^2)/2}$.
In this specific case the value $n_{top} = 1.309$ RIU (*RIU = refractive index units*) was chosen which was found in optimization to give a high ratio of left/right-scattered intensities. This value of refractive index is rather close to that of water which is favourably since the refractometric sensing is generally conducted in water-like mediums. The refractive index of the lower medium was taken as for glass $n_g = 1.5$ RIU. This results in an effective refractive index of $n_{eff} = 1.4077$ RIU.

Incident linearly x-polarized light, propagating in the direction of negative z-axis, was then used to excite dipoles on the spheroids. The polarizability functions of the two different spheroids are calculated using equation (2.20) with the geometrical form factor calculated according to equation (2.7) and frequency dependent dielectric function $\epsilon(\omega)$ was taken from experimental values for Au [17]. With this information it was straight forward to use equations (2.11) and (2.12) to calculate the scattering- and absorption cross sections which is illustrated in Figure 2.5. From these figures it is clear that the spectra yields two distinct localized plasmon resonance peaks properly detuned from each other.
Moreover equation (2.22) was used to simulate coupling effects between the dipoles. Hence the magnitudes and intrinsic phase difference could be found for the spheroids which is shown in Figure 2.6. Finally the ratio of the left/right-scattered intensities, along the dimer axis, were calculated according to equation (2.25). The result is demonstrated in Figure 2.7 and shows a very high directionality with a ratio of $R_I = 2.791 \cdot 10^4$ at $\lambda = 680$ nm.

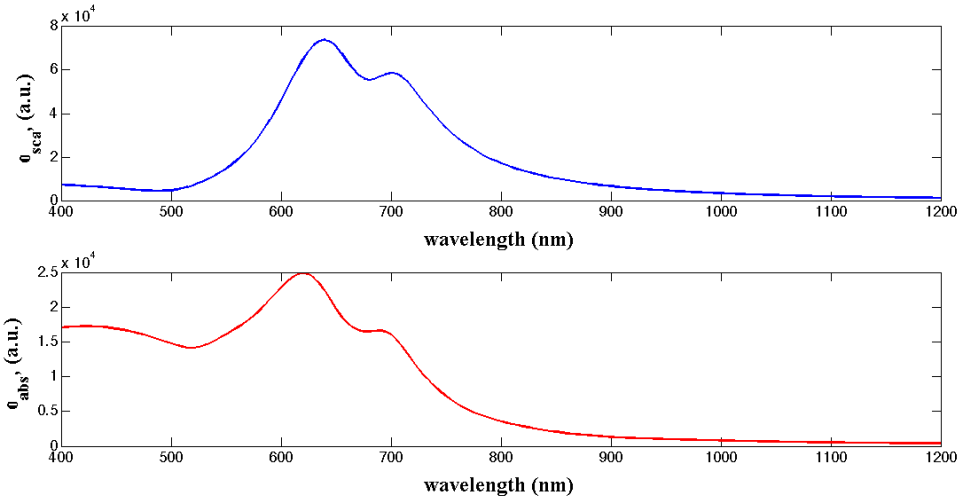

Figure 2.5: *Simulated scattering- and absorption cross sections.*

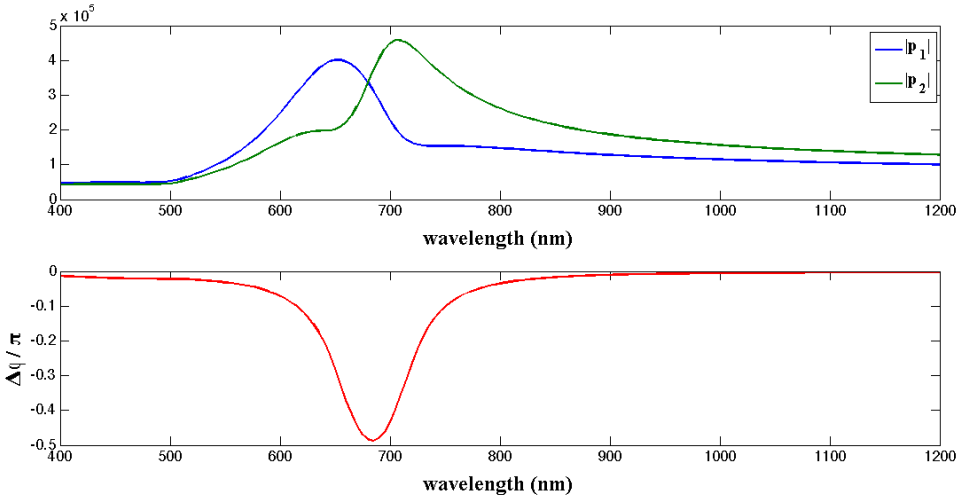

Figure 2.6: *Simulated magnitude and intrinsic phase difference (in unit steps of π radians) of the different dipoles. Note that the difference in intrinsic phase is around $-\pi/2$ for the same wavelength where the magnitudes of the two dipoles coincide ($|\boldsymbol{p}_1| = |\boldsymbol{p}_2|$).*

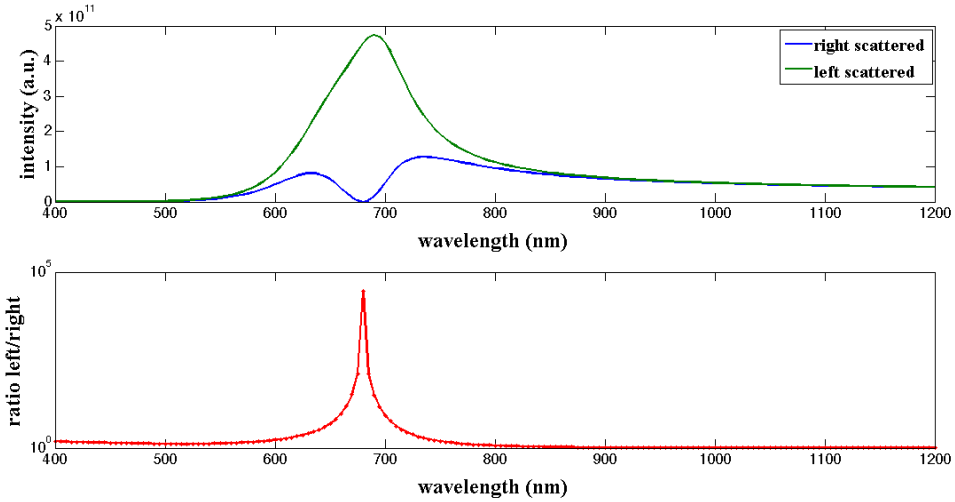

Figure 2.7: *Simulated magnitude and ratio of intensities scattered to left/right along the dimer axis. Notice the logarithmic scale on the graph showing the ratio of scattered intensities.*

3

Sensing with plasmonic nanoparticles

Plasmonic nanoparticles yields great potential in acting as future sensors. Due to factors like its nanoscale spatial dimensions and sensitivity to local environmental changes, they show very promising applications in both material industries and biomedical science. The current methods and upcoming trends for using nanosized plasmonic particles as sensors are briefly described in this section.

3.1 General methods for plasmonic sensing

As described earlier, plasmons are highly sensitive to dielectric changes in their local environment. How sensitive a certain plasmonic nanoparticle is to ambient environmental changes depends on several factors like geometry and material composition, but also the ease of electron polarization in the nanoparticle.
In the field of plasmonic sensing one often distinguishes between *bulk sensing* and *local sensing*. In the bulk sensing model one assumes that the total ambient environment, in which the nanoparticles are located, is replaced by a medium with different dielectric properties. In local sensing it is assumed that the dielectric properties changes only within a region of the probe volume V_p around the nanoparticle. By assigning the spatial range of the probing region with a parameter d_p one clearly sees that the local sensing model converges to the bulk sensing model when $d_p \to \infty$. The simplest way of determining the plasmonic signals in these two sensing platforms are done in the bulk model. To quantify how sensitive a certain model is to dielectric changes of the ambient environment it is convenient to define parameters like *sensitivity* and *figure of merit* (FOM). The first quantity is simply defined as $\partial\lambda_{LSPR}/\partial n$ where λ_{LSPR} is the LSPR wavelength and n the refractive index of the surrounding medium. This means simply that the sensitivity aspect describes the change in resonance wavelength for a unit change in the

refractive index of the ambient medium.
Further analytical investigation shows that the sensitivity of a sub-wavelength nanoantenna can be written as

$$\frac{\partial \lambda_{LSPR}}{\partial n} = \frac{2Re\{\epsilon(\lambda)\}}{n} \frac{\partial Re\{\epsilon(\lambda)\}}{\partial \lambda}\bigg|_{\lambda=\lambda_{LSPR}} \tag{3.1}$$

where $\epsilon(\lambda)$ is the wavelength dependent dielectric function described in the previous chapters. A typical sensitivity for gold nanodisks are around 200 nm/RIU [1].
Even though this sensitivity quantity plays a crucial role in sensing measurements it doesn't say anything about the sharpness of the resonance peak, neither give any information about *spectroscopic contrast*. Hence, a useful definition to add when describing the sensitivity aspect is the figure of merit (FOM) which is defined by

$$FOM = \frac{1}{\Delta\lambda_{1/2}} \frac{\partial \lambda_{LSPR}}{\partial n} \tag{3.2}$$

where $\Delta\lambda_{1/2}$ describes the *full width half maximum* (FWHM) of the Lorentzian shaped resonance peak.
Even though a certain nanoparticle yields highly sensitivity property according to equation (3.1) it can still show a mediocre value of FOM. Since broadening of the plasmon resonance peak occurs due to radiative damping, see equation (2.20), FOM is a very important measure of sensitivity.

Another very important aspect to take in to account, when studying immobilized plasmonic nanoparticles on a substrate, is the fact that the surface area are different from free colloidal nanoparticles. This results in a symmetry breaking around the nanoparticle and affects the charge distribution on which the plasmon resonance heavily depends. Furthermore, in the case of the sensing aspect, fewer molecules can bind to the nanoparticle with less surface area exposed to the ambient medium.

The previuosly described sensing platforms are the most widely used and studied at present. However there are some recently alternative sensing schemes worth mentioning. First and foremost Becker *et al.* describes an alternative FOM quantity than what is shown in equation (3.2). Instead of resonance peak position this model focuses on amplitude of the resonance peak [7]. This alternative FOM is explicitly described as

$$FOM^* = max\left|\frac{1}{I_0(\lambda)} \frac{\partial I(\lambda)}{\partial n}\right| \tag{3.3}$$

where $I(\lambda)$ is the wavelength dependent intensity, n refractive index and $I_0(\lambda)$ a reference signal.
An additional sensing scheme were demonstrated by Evlyukhin *et al.* [9] where they considered a sample consisting of several slightly detuned dipole-pair nanoantennas. Due to spatial- and intrinsic phase retardation, between the dipoles in the pair, high

directional scattering effects was acquired. This phenomena arises due to that dipoles in the pair configurations interfere constructively in one direction, while simultaneously interfering destructively in the opposite direction. By then measuring the ratio between the scattered intensities along the right/left of the dipole-pair axis one will acquire a high sensing contrast.
This base was also used by Shegai *et al.* [2] to demonstrate hydrogen sensing in a Pd/Au dimer sample. After locating the wavelength where the maximum directionality occurs they used a single wavelength light source and changed the hydrogen partial pressure in the ambient environment of the dimers. By this strategy a change in ratio of $\Delta R_I \approx 1.4$ was achieved by alter the hydrogen partial pressure by a few millibars.

3.2 Converting shift in plasmon resonance to amount of detected molecules

A crucial property of a sensor is to determine the amount of substance (molecules) that are present in the close environment of the nanoparticles. As we can see from equation (2.10), the LSPR frequency shifts if the local dielectric environment changes. It turns out that it is possible to relate the amount of adsorbed molecules to the LSPR shift according to $\Delta\lambda_{LSPR} = \Delta n_{eff}\frac{\delta\lambda_{LSPR}}{\delta n}$, where $\frac{\delta\lambda_{LSPR}}{\delta n}$ is called the *bulk sensitivity* and Δn_{eff} is the effective refractive index. Furthermore Δn_{eff} can be expressed as

$$\Delta n_{eff} = \frac{1}{l_d}\int_0^\infty (n(z) - n_d)\mathrm{e}^{-2z/l_d}\,\mathrm{d}z \tag{3.4}$$

where n_d is the refractive index of the surrounding medium and $n(z)$ the refractive index a distance z away from the nanoparticle. The parameter l_d is the field decay length which is related to the plasmon wavelength, where $l_d \approx 28$ nm for low aspect ratio nanodisks. In the case of detecting proteins, the change in refractive index can be quite easily converted to the surface mass density Γ of a certain protein layer. This is done according to

$$\Gamma = \frac{d_p \Delta n_{eff}}{\delta n/\delta c} \tag{3.5}$$

which is also known as Feijters formula. Here d_p describes the thickness of the protein layer and $\delta n/\delta c$ is known as *biomolecule refractive increment* which has a value around 0.182 $\mathrm{cm^3 g^{-1}}$ for most proteins [1].

3.3 Sensitivity aspect of directional-scattering-ratio plasmonic sensing

A central issue with a lot of the previously presented sensing schemes is that they require either microscopes or spectrometers which are both expensive and takes up valuable space. These factors are very limiting and/or impractical when considering a system aimed to work as a biosensing device.

It is moreover important to search for different ways to overcome the limited sensitivity which can be achieved with present sensitivity platforms such as change in LSPR wavelength for a unit change of refractive index (see equation 3.1).
Inspiration is now taken from several ideas presented in work done by both Evlyukhin *et al.* and Shegai *et al.* which, as previously mentioned, made use of directional scattering by asymmetric monometallic/bimetallic nanosized dimers for acquiring high sensitivity [2], [9]. By studying the ratio R_I (see equation (2.25)) of the scattered intensities for a single wavelength light source it is possible to reach enormously high *directional scattering resonance sensitivity* ξ_{DRS} by measuring the quantity

$$\xi_{DRS} = \left.\frac{\partial R_I}{\partial n}\right|_{\lambda=const} \tag{3.6}$$

i.e. the change in "directional resonant behavior" for a unit change in refractive index. A comparison between "ordinary" LSPR shift refractometric plasmonic sensitivity and "directional resonance" sensitivity can be seen in Figure 3.1, based on theoretical simulations performed in a similar manner as in Figure 2.7. While the "ordinary" refractometric LSPR shift sensitivity, in Figure 3.1 (b), gives a value of $\partial\lambda_{LSPR}/\partial n \approx 100$ nm/RIU the "directional resonance" sensitivity, in Figure 3.1 (d), shows a value of $\xi_{DRS} \approx 8.84{\cdot}10^6$ RIU^{-1} around $n = 1.4$. This is almost a factor of 10^5 higher which is an indication that refractometric measurements, based on directional scattering, is a very promising sensing platform.
By further investigating the slope of the curves in Figures 3.1 (b) and (d) it is moreover clear that the LSPR shift sensitivity remains at a constant value around 100 nm/RIU for each value of refractive index, whereas the "directional resonance" sensitivity ξ_{DRS} is highly dependent on refractive index. This furthermore implies that it is possible to tune the dimer system in such a manner that the highest achievable sensitivity region occurs for refractive indices corresponding to that of physiological buffers. These measurements are generally conducted using substances with a refractive index in the range $n = 1.33$ - 1.4 [27].

However there are some limiting factors worth considering when performing directional sensing. For example the background signal which originates from straylight, induced by the glass substrate and the rest of the optical path from light source to detector, will decrease the ratio of the left/right-scattered intensities immensely if not subtracted. The performance of this subtraction is not obvious to do due to the fact that it can cause negative values for some wavelengths since the straylight from a blank clean glass slide will yield a higher transmission than a glass slide with nanodimers positioned on top. Therefore a fraction of the straylight spectrum needs to be subtracted which is estimated from the decrease in transmission caused by the surface area occupied by the nanodimers [2]. Since this straylight subtraction is crucial in order to achieve the "true" scattering ratio values this is quite a drawback for this sensing scheme. More details about the impact of straylight on left/right-scattered intensities is described in the Chapter 5 as well as in Appendix A.1 at the end of this report.

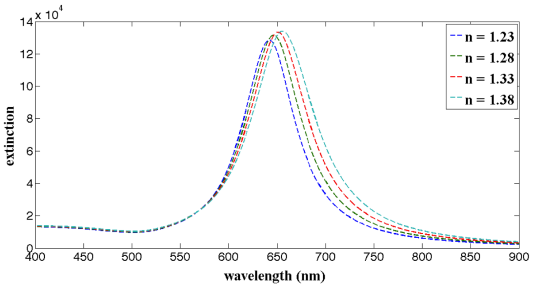

(a) *Extinction spectra for some different refractive indices. Notice that the the peak position shifts to the red with increasing refractive index.*

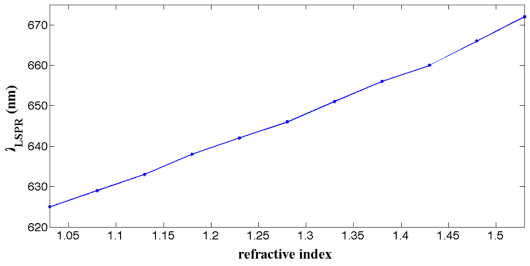

(b) *Localized surface plasmon resonance wavelength λ_{LSPR} vs refractive index. This sensitivity aspect is the basis for many of the present sensing platforms which uses plasmon resonances.*

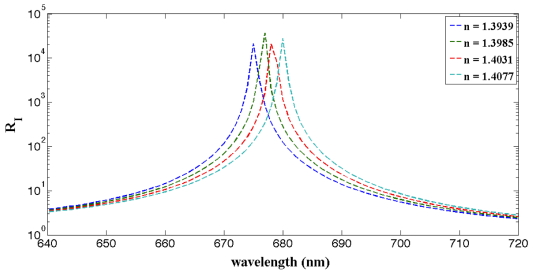

(c) *Ratio spectra for four different refractive indices. The peak of the green curve is located at 677 nm and is used as a single wavelength reference in the graph to the right. Notice the logarithmic scale on the y-axis.*

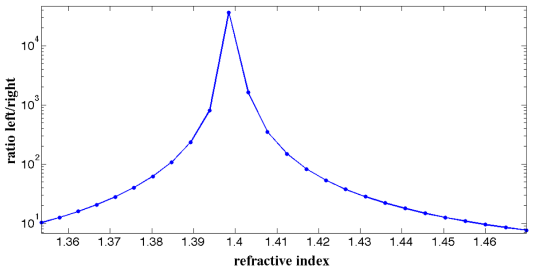

(d) *An illustration of how the ratio of scattered intensities changes with effective refractive index n_{eff} at a constant wavelength of $\lambda = 677$ nm. Note the logarithmic scale on the y-axis.*

Figure 3.1: *Comparing the LSPR peak shift platform of plasmonic sensing with a new platform based on directional scattering.*

4

Experimental results

The core of this project is experimental examination and evaluation of a new type of optical setup which is both self-referenced and microscope-free. This chapter is dedicated to illustrate the manufacturing process of the dimer samples as well as highlighting the sensitivity, rigidity and simplicity of the self-made microscope-free optical setup. Generally we want to present and discuss the biosensing ability of a system which make use of directional scattering effects from monometallic Au nanodimers.

4.1 Manufacturing process of asymmetric Au nanodimers

The samples, containing the Au dimer disks, are manufactured by using the hole-mask colloidal lithography (HCL) method. This manufacturing method can briefly be illustrated in a few different steps.

First of all, a flat circular substrate made of a high refractive index medium (glass, quartz etc.) is used. A film of polymethyl metacrylate (PMMA) is then put on top of this substrate with a method called spin-coating which uses centrifugal force to spread out the PMMA creating an homogeneously thick film over the substrate [18]. This is done by placing an excess amount of PMMA on the substrate and connect it to a rotor. Due to this setup one can tune the thickness of the film by adjusting the angular velocity of the rotor attached to the circular substrate. Thereafter a very quick oxygen plasma etch is done in order to increase the hydrophilic property of the film.

Next a water suspended positively charged polyelectrolyte is put on to the PMMA layer forming a very thin adhesive film on its surface. In addition to this a colloidal solution containing negatively charged polystirene beads are placed on top of the adhesive film, causing an attractive force between the layer and the film and a repulsive force between

the polystirene beads. The result of this is that the beads sticks to the film at locations sufficiently far apart from the neighbouring beads.

The following step in this process is to deposit a very thin film of a substance which can resist the later etch with the highly reactive oxygen plasma which is used to form holes in the PMMA layer. Before the oxygen plasma etching takes place the polystirene beads are taken away using adhesive tape. It is the absence of these beads which leaves small holes creating the so called hole-mask on top of the PMMA film.

Furthermore, gold is evaporated from an external source from two different angles of incidence creating dimer disks in the holes made by the oxygen plasma etching. The angles of incidence are chosen depending on the desired intermediate spacing between the dimer disks, and the height/width is controlled by evaporation time and the amount of over-etch [19]. The overall scheme for this manufacturing process can be viewed in Figure 4.1.

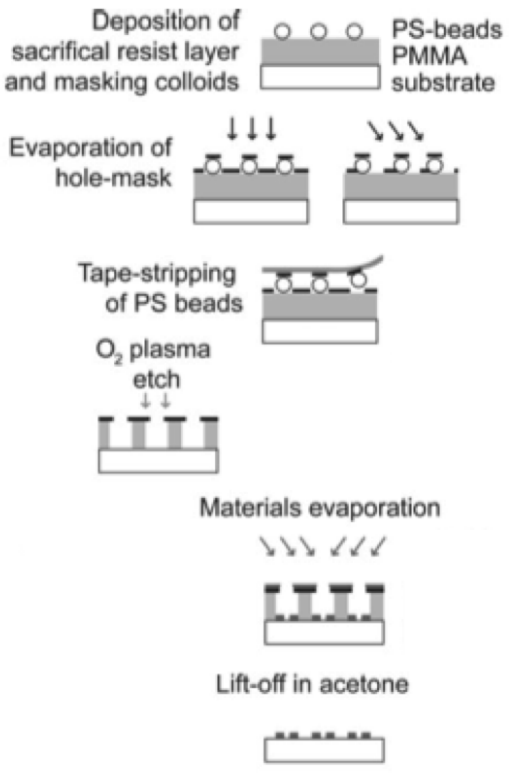

Figure 4.1: *Schematic drawing of the different steps in the hole-mask colloidal lithography method. Picture taken from [19].*

4.2 Determining geometrical dimensions of Au dimers with SEM measurements

The result from the manufacturing process using the hole-mask colloidal lithography method, described in previous chapter, is shown in Figure 4.2 which is an image taken in environmental scanning electron microscope (ESEM). We can clearly see that the sample contains asymmetric dimer pairs all oriented in the same direction. The geometric

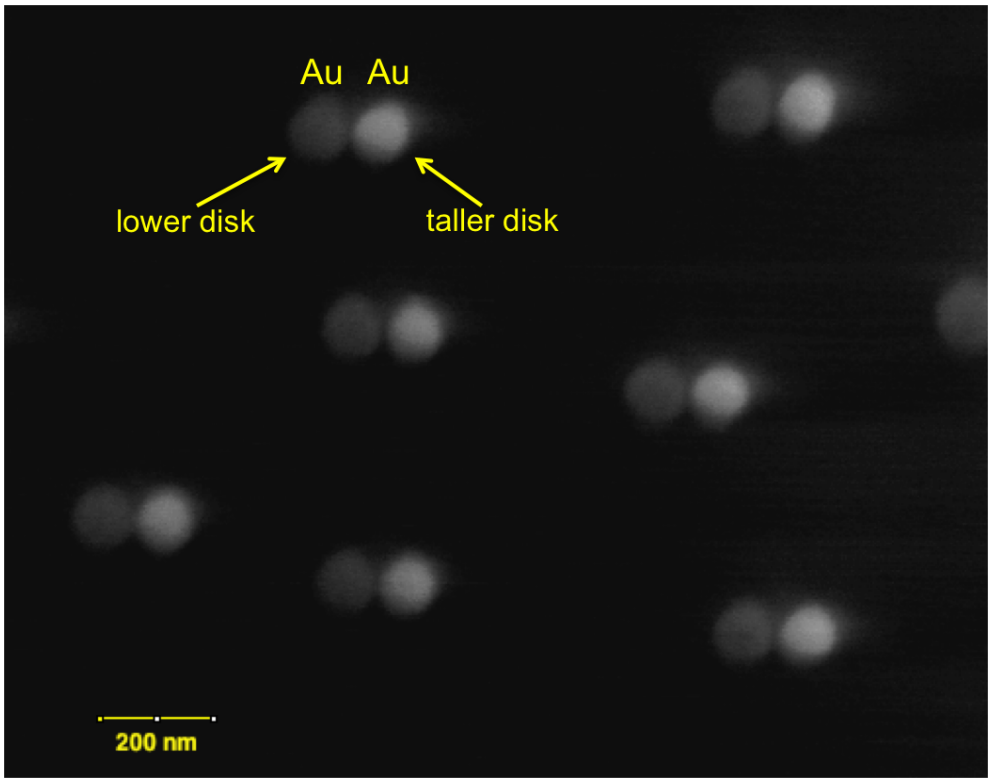

Figure 4.2: *SEM image showing the structure of the dimers which was manufactured through the hole-mask colloidal lithography method. The height difference appear as a difference in brightness between the dimer disks.*

dimensions of the dimer disks in Figure 4.2 was analyzed through statistical measuring in the imaging processing software *ImageJ*, and was found to be $D_1 = 103.67 \pm 4.75$ nm for the lower Au disk, $D_2 = 100.65 \pm 5.89$ nm of the taller Au disk and an intermediate gap size of $d = 11.85 \pm 2.61$ nm after boiling in TL 1 and heated during the annealing process. This gives a center-to-center distance of $L = 114.01 \pm 7.93$ nm.
It is not possible to determine the exact height of the dimer disks from the SEM measurements, but one clearly see by contrast that there is a height difference (one is brighter than the other). Additional measurements in atomic force microscopy (AFM) would have been necessary in order to determine the exact height difference [20]. But since the extinction spectra showed signs of directional scattering samples, this step was consid-

ered as non-crucial for this study.

4.3 Locating plasmon resonances in extinction spectra

Since the measurements highly depends on plasmonic properties of the nanodimers, it is very important that the LSPR occur at the expected wavelengths. A very straight forward method to observe the spectral positions and magnitudes of plasmonic resonances is to measure the extinction spectrum of the sample. Via the information in these spectra, it is possible to draw conclusions about eventual directionality effects by studying the detuning of the resonance peaks. Closely spaced asymmetric dimers should also show different response, to incident light which is polarized perpendicular to the dimer axis than light with a parallel polarization. Therefore it is also possible to determine if the distances between the dimer disks are too large in order for the interaction between dipoles to occur.
Extinction spectra for dimers with dimensions $D_1 = 103.67 \pm 4.75$ nm, $D_2 = 100.65 \pm 5.89$ nm, $h_1 = 26$ nm, $h_2 = 62$ nm and an intermediate center-to-center distance of $L = 114.01 \pm 7.93$ nm, can be viewed in Figure 4.3 (a). These spectra are measured over the visible- and part of the infrared range of the electromagnetic spectrum. These measurements are conducted in a spectrophotometer (Cary 5000 UV-Vis-NIR Spectrophotometer) where the polarization of the incident light are varied with a linear polarizer. From these spectra one cannot really distinguish two distinct resonance peaks, which is a crucial property for directional scattering. However, neither of the two resonance peaks has an ordinary Lorentzian shape which implies that we can suspect the presence of two peaks, but they are either too close in wavelength and/or too broad to be distinguished as separate peaks. It turns out that a quick and easy chemical treatment of the samples can be made in order to improve both the separation and narrowing of the peaks. This is simply done by boiling the samples in a chemical substance called TL 1 and further annealing them on a heater which is described in the next subsection.

4.3.1 Improving resonance peaks with TL1 and annealing

To further improve the detuning and narrowing of the resonance peaks the samples were put in a bath of TL 1 which contains of 20 ml of distilled water (H_2O), 5 ml of hydrogen peroxide (H_2O_2) and 5 ml of ammonia (NH_3). This mixture together with the sample were put in a beaker and boiled in 150^oC for 3 minutes. Since Au is chemically inert to this substance it mainly results in a thorough cleaning of the samples from organic molecules [21]. After this procedure the nanosample were rinsed with distilled water and afterwards dried with nitrogen gas.
Thereafter the dried sample was put on a heater to be annealed in 250^oC for 10 minutes. This process smoothen the Au dimer disks and reduces sharp inhomogeneities on the disk surfaces which can be sources of broadening when studying the extinction spectrum. Furthermore annealing also improves the crystallinity of the material which proves to be another eligible property for improving the features of the resonance peaks in the

extinction spectrum. The most plausible reason for this is; before the process of annealing occurs the Au disks are not really homogeneous inside but is a composition of several grains of varying sizes. However some of these grains may be comparable to the mean free path of the conduction electrons, causing perturbations and further broadening of the plasmon resonance peaks. Due to the heat produced during the annealing process these grains will become significantly bigger in size, and more well defined narrower peaks will be present in the extinction spectrum.
The spectra for the same sample as Figure 4.3 (a) shows, after boiling in TL 1 and annealed, is illustrated in Figure 4.3 (b). It clearly shows that the resonance peaks have blueshifted and narrowed immensely. In this case it is moreover obvious that two distinguishable peaks appear when the incident light is polarized perpendicular to the dimer axis. According to theoretical estimations from Figures 2.5 and 2.7, the highest directionality effect should occur at a wavelength in the spectrum where the dip between the detuned resonance peaks occur. In Figure 4.3 (b) it is obvious that this dip occur somewhere around $610 - 620$ nm. The highest scattering directionality is therefore expected to be observed in this region.

4.3.2 Measuring scattering in opposite directions in the microscope Fourier plane

It turns out that it is actually possible to see the effect of directional scattering by eye, without using any spectrometer. By placing the sample in a microscope (Nikon Eclipse TE2000-E) and switch from the real image to the Fourier image plane, one can study the angular distribution of scattered light. The principle for the microscope Fourier plane is illustrated in Figure 4.4 (a). The result in angular scattering for the Au nanodimer sample after TL 1 and annealing can be seen in Figure 4.4 (b), which illustrates how different colours scatters in different angular directions with varied intensities. These measurements corresponds to a situation where the Au dimers are located in air. It is clear from Figure 4.4 (b) that the left-scattered light is more intense with a reddish colour while the right-scattered light contains of less intense greenish/yellowish light.
This result seems to be in quite good agreement with what was observed in the extinction spectrum (Figure 4.3 (b)), with a directionality effect in the near infrared regime.
Moreover it is possible to view differences in the Fourier plane if the Au dimers are located in water instead of air. According to equation (2.16), the forbidden zone changes when the refractive index of the upper medium changes. Since water has a higher refractive index than air we would expect the forbidden zone to be more narrow and occurring at a higher scattering angle. An illustration of how this change looks like can be seen in Figure 4.5 with and without an optical filter (650 ± 20 nm). Moreover Figure 4.5 (a) shows two inset figures which corresponds to the Fourier plane image of a clean glass slide. These figures shows the amount of straylight which originates from the sample substrate. This needs to be taken in consideration when measuring the scattered light from the Au dimers. A measurement of the spectrum of both left/right-scattered light, in the microscope Fourier plane, was conducted to quantify the amount of directionality that was present. Moreover the contribution of straylight was measured for both right/left-

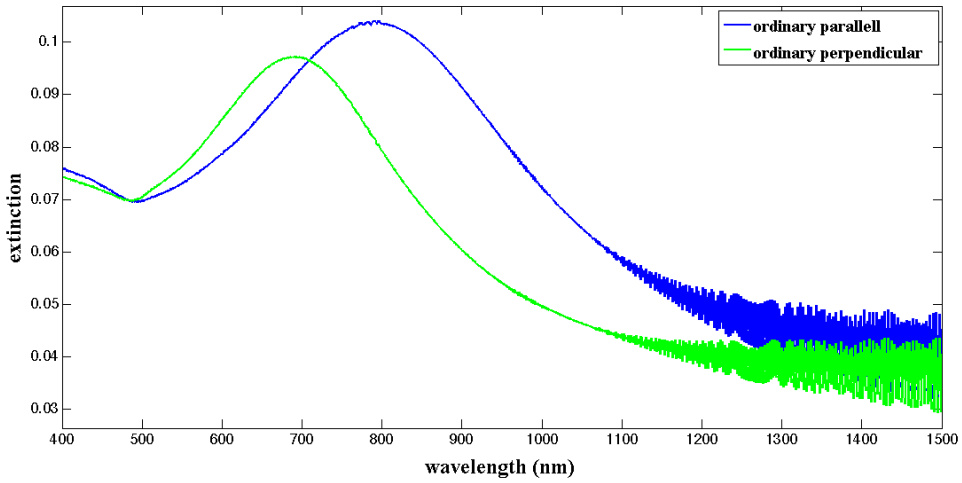

(a) *Extinction spectra for Au nanodimers with dimensions* $D_1 = 103.67 \pm 4.75$ *nm,* $D_2 = 100.65 \pm 5.89$ *nm,* $h_1 = 26$ *nm,* $h_2 = 62$ *nm and an intermediate center-to-center distance of* $L = 114.01 \pm 7.93$ *nm. The blue curve corresponds to incident light with parallel polarization and the green curve to perpendicular polarization with respect to the dimer axis.*

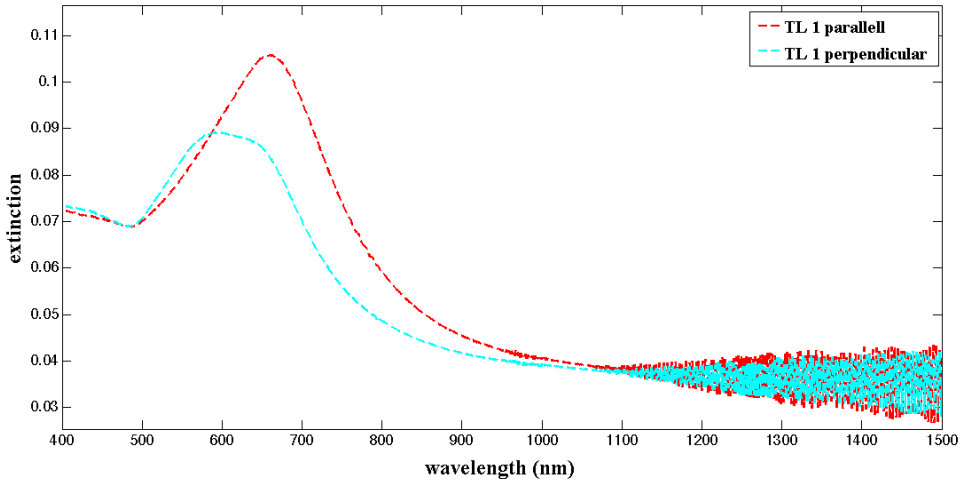

(b) *Extinction spectra which shows the result of boiling the samples in TL 1 and annealing them on a heater. Note the distinct two peaks that suddenly appears when incident light with perpendicular polarization is used.*

Figure 4.3: *An illustration of how the extinction spectra changes after the nano dimers have been boiled in TL 1 and annealed on a heater.*

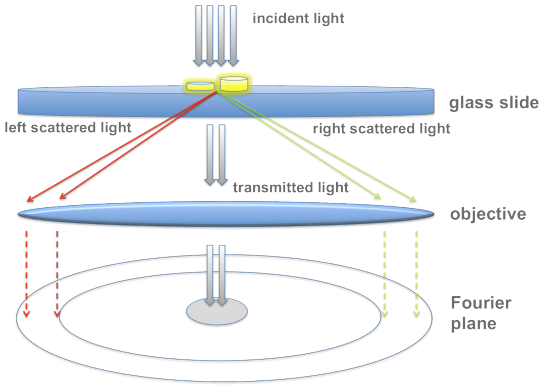

(a) *Figure illustrating the principle of the microscope Fourier plane. The dimers are positioned in the objective focal plane and the scattered light is projected as a 2D image illustrating angular scattering. Notice that the relation of the dimensions between the Au dimers and the glass slide is highly exaggerated.*

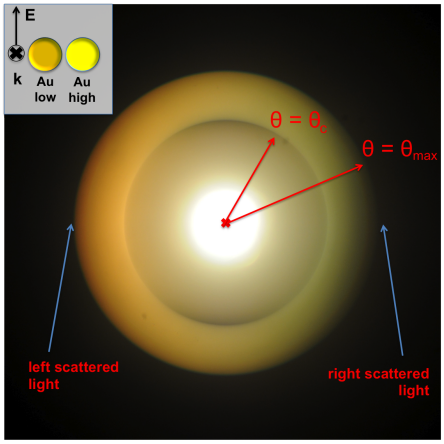

(b) *Fourier image plane of the sample after TL 1 and annealing. The orientation of the dimers and polarization of the incident light are marked in the inset figure. It is clear that the left-scattered light is more intense with a reddish colour while the right-scattered light contains of less intense greenish/yellowish light.*

Figure 4.4: *An illustration of the microscope Fourier plane image and the angular scattering of the Au nano dimer sample.*

scattered light and subtracted from the corresponding spectra. These spectra can be seen in Figure 4.6 which shows that the highest amount of directionality occurs at a wavelength around 614 nm in air and around 680 nm in water.

4.4 Microscope-free optical experimental setup

The final aim for this project is to build a system which can measure the ratio of intensities, scattered in opposite directions along the dimer axis, from the radiating nanodimers. Here one may take advantage of the previously described radiation pattern (see equation (2.16)) that arises from dipoles located near a plane interface. When the plasmonic disks are located very close to the plane surface the exponentially decaying evanescent fields which originates from the excited dipoles may couple to the optically denser lower medium and be transformed into propagating modes. This phenomena is generally referred to as optical tunneling [4].
The samples consists of Au nanodimers with disk heights of $h_1 = 26$ nm and $h_2 = 62$ nm with local surface plasmon resonances around $\lambda_{LSPR} = 580-650$ nm. By approximating these disks as radiating point dipole sources, located at the center of each disk, the height of the dipoles over the plane surface fulfills the condition $\lambda/100 < \frac{1}{2}\{h_1, h_2\} < \lambda/10$

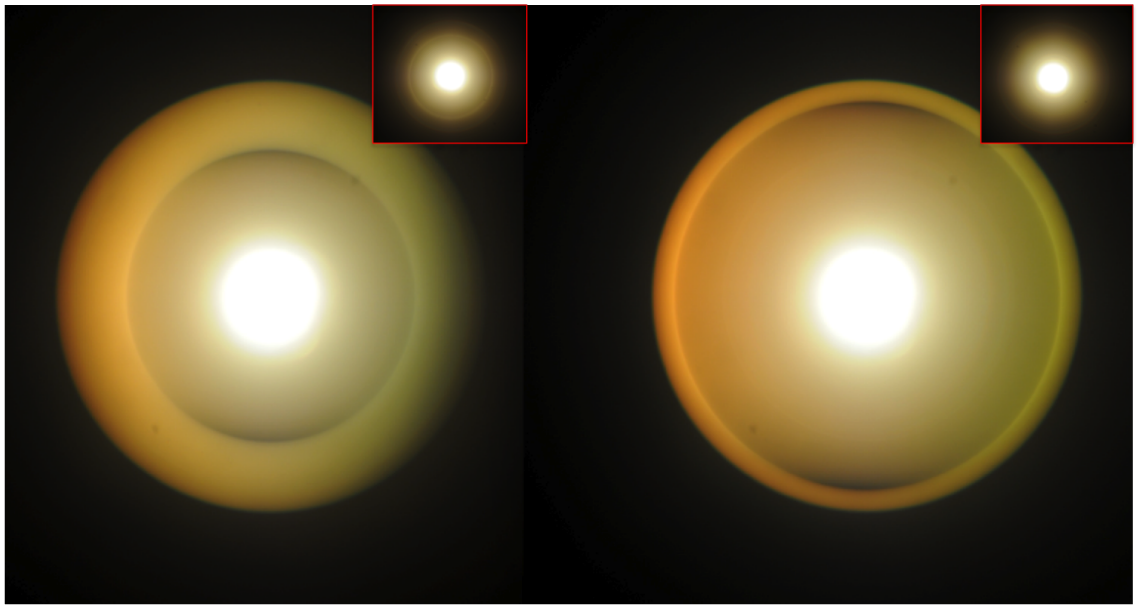

(a) *Fourier image showing how the forbidden zone changes when the Au dimers are located in water (right image) instead of air (left image). The inset figures shows the Fourier plane image for a clean glass slide which illustrated the amount of straylight which originates from the substrate in each dielectric environments.*

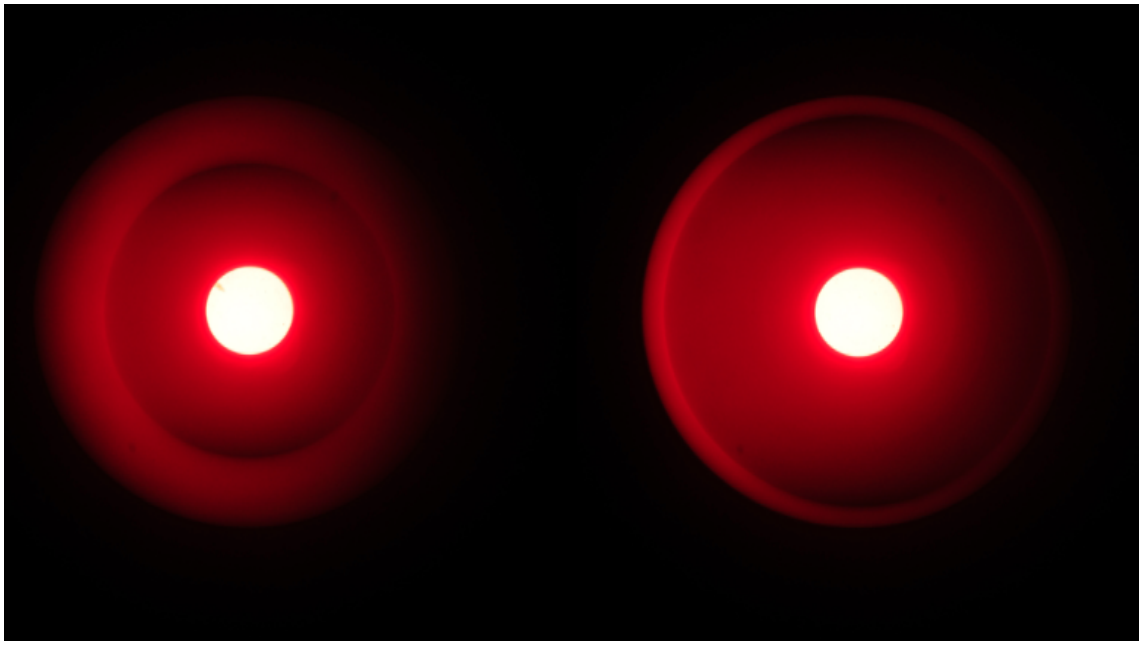

(b) *Fourier image when an optical filter of* 650 ± 20 *nm have been used. These images clearly illustrates that red light scatters significantly more to the left than to the right both in air and in water.*

Figure 4.5: *A comparison of how the angular scattering changes when the Au dimers are located in water instead of air.*

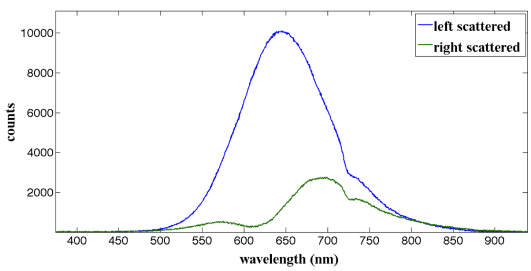

(a) *Scattering spectra measured in the Fourier plane with subtracted straylight. This spectra corresponds to the situation when the nanodimers are located in air.*

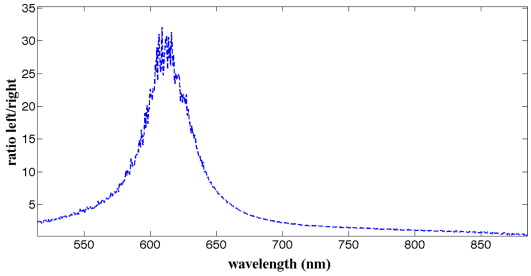

(b) *Ratio of the left/right-scattered intensities when the nano dimers are located in air.*

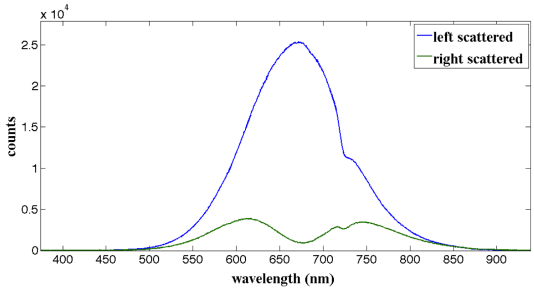

(c) *Scattering spectra measured in the Fourier plane with subtracted straylight. These spectra corresponds to the situation when the nano dimers are located in water.*

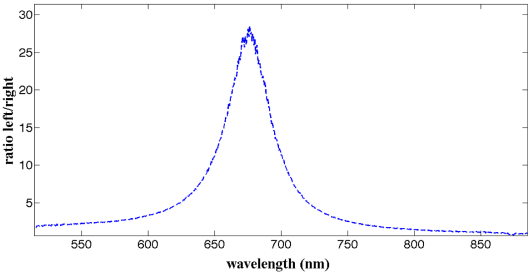

(d) *Ratio of the left/right-scattered intensities when the nano dimers are located in water.*

Figure 4.6: *Intensity spectra measured in opposite directions in the microscope Fourier plane, both for upper medium of air and water.*

which indicates that a significant part of the scattered light will be concentrated in the forbidden zone. By placing these samples on top of a hemispherical prism, with a thin layer of immersion oil in between, the system behaves as if the nanodimers were located directly on the prism.

Due to the fact that the scattered light waves will propagate in a direction at an angle $\theta_e \geq \theta_c$ with respect to the normal vector of the top plane surface of the hemispherical prism, two detectors are placed with their center located an angle $\theta \in \{\theta_c, \theta_{max}\}$ (see Figure 4.4). These detectors will then register an average of the left/right-scattered light into the forbidden zone. The schematic concept of the setup is illustrated in Figure 4.7. Furthermore this setup filters out the light which is located in the allowed zone (transmitted light and scattered light which originates from dipoles located far away from the upper plane glass surface) which is very much beneficial for the sensing aspect of this study.

In order to get parallel incident light the light source consisted of a fiber connected to a halogen lamp in one end and to a collimator in the other end. Since the highest

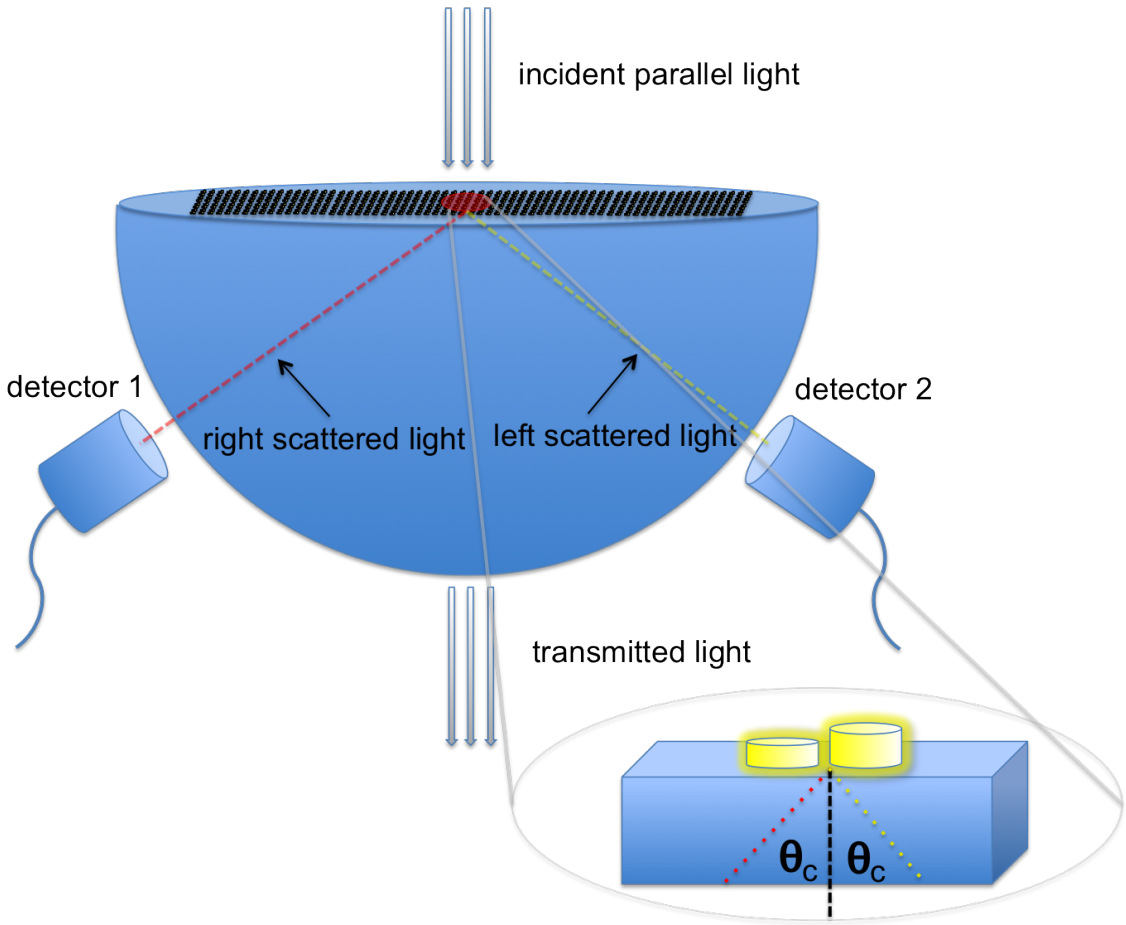

Figure 4.7: *A sketch of the microscope-free optical setup. Scattered light from the dimers radiates at an angle bigger or equal to θ_c. The lower part of the figure shows a magnified image of the nanosized Au dimers.*

directionality occurs when the incident is polarized perpendicular with respect to the dimer axis, a linear polarizer was placed directly after the collimator. Another suitable property for an optical system is the ability to control the spot size of the incident beam. This indicates that an aperture is needed. The optical setup can be viewed in Figure 4.8 (a) which points out the different parts of the system. Furthermore we can view the result of the directionality effect from the asymmetric nanodimers in Figure 4.8 (b), where two distinct different colours appears when sheets of paper are placed in front of each detector. From this image it is quite clear that the microscope-free optical system reproduces the Fourier plane image in Figure 4.4. This is a very nice indication that the optical setup works well for measuring the directional scattering effect for a certain sample.
An alternative microscope-free optical setup is presented in Appendix A.2 at the end of this report. However this setup needs further improvement in terms of noise reduction

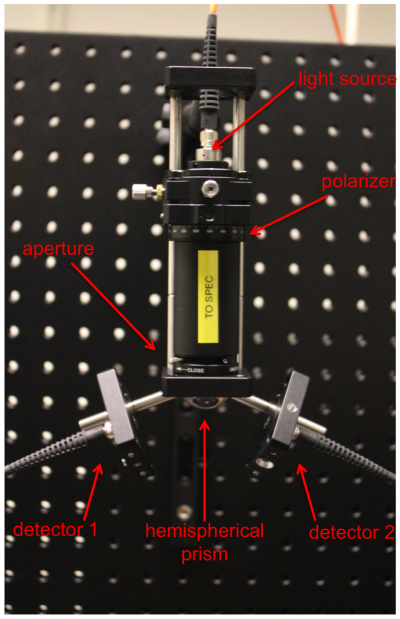

(a) *A picture showing the optical setup. A one inch circular sample containing Au dimers is placed on top of the hemispherical prism with a thin layer of immersion oil in between. Detectors 1 and 2 detects the scattered light.*

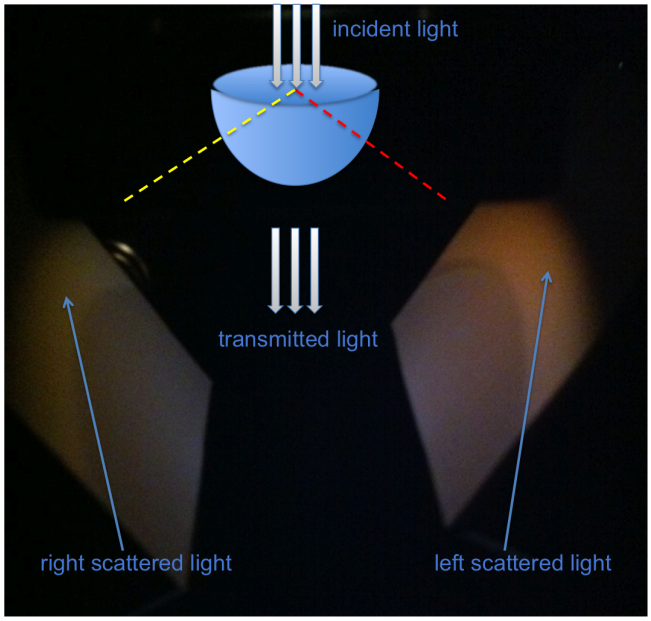

(b) *A photograph of the colours observed by placing white paper sheets in front of each detector. The position of the hemispherical prism is drawn in order to compare with the left image. One can really view the directional scattering by comparing the right/left-scattered light.*

Figure 4.8: *Illustration of the different components in the microscope-free optical setup and an image showing the directionality effect.*

to be comparable with the setup described in this section.

4.4.1 Testing the validity of the microscope-free optical experimental setup

In order to verify that the optical setup, in Figure 4.8, gives reliable signals it was necessary to first conduct measurements on a sample which absorption spectra was previously known.
The test sample consisted of monometallic Au monomers (see Figure 4.9 (a)), with a mean diameter of $D \approx 110$ nm. Since monomers have rather symmetric geometrical features there should be no sign of directionality in the scattered intensities which can be seen from the Fourier plane image illustrated in Figure 4.9 (c). This moreover means that the amount of intensity detected in right/left detectors should be the same over the whole spectral region which seems to be the case according to Figure 4.9 (b) and (d). All these measurements were carried out using a spectrometer (Andor SR-3031-B). The data for Figures 4.9 (b) and (d) was acquired by accumulations of 10×1 seconds

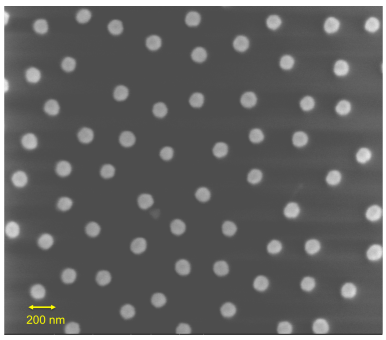

(a) *SEM image of the monomer Au sample which was used as a test for the optical setup.*

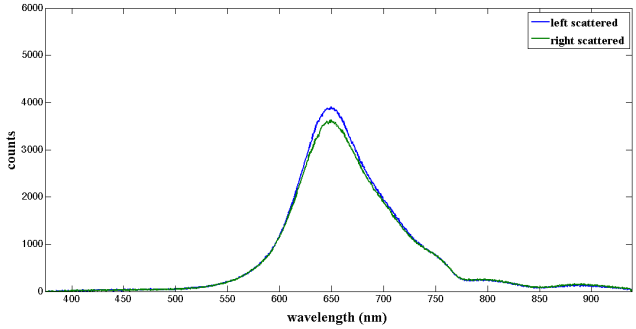

(b) *Figure illustrating the left/right-scattered light for the monomer sample. This figure shows that the microscope-free setup produces reliable information since the curves coincide rather well for each wavelength.*

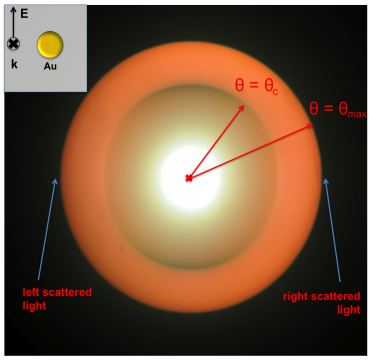

(c) *A Fourier plane picture taken for the monomer sample which shows the symmetry in angular scattering.*

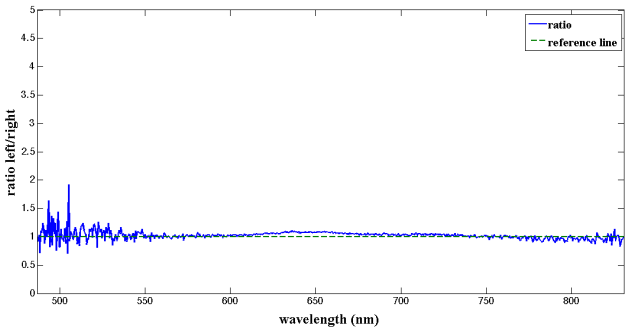

(d) *Ratio of left/right-scattered intensities. It is clear that no directional scattering occurs since the ratio is close to one over the whole spectral region.*

Figure 4.9: *Images showing the reliability for the microscope-free optical setup.*

integration time with background correction. The background was measured in each detector when the light source was switched off.

4.4.2 Using scattering directionality from asymmetric Au dimers for bulk refractive index sensing in a microscope-free optical setup

As stated many times earlier in this report, the final aim in this project is to perform sensing experiments in a microscope-free setup using directional scattering effects, rather than relying on ”ordinary” sensing platforms based on LSPR peak shift measurements. In the case of altering the dielectric properties in the ambient medium and simultaneously measuring ratios of left/right-scattered intensities, it is very much important that the location of the measuring detector is stable. When measuring the scattered intensities in the Fourier plane of the microscope (see Figure 4.6) one has to position the detecting

fiber each time the focus has been adjusted. Hence the detector needs to be repositioned every time a change in the refractive index of the ambient medium is performed.
However in the microscope-free optical setup the detectors are screwed tightly on to rails and can be adjusted in radial-, ϕ- and θ-directions (see Figure 4.8 (a)).
The change in refractive index of the ambient medium was conducted by mixing a specific amount of ethylene glycol ($C_2H_6O_2$) in distilled water (H_2O). An increase in refractive index of $\Delta n = 0.01$ corresponds to an 10 percent increase in ethylene glycol concentration [22].
The experiment was performed by first measuring the scattered intensities when the dimers were located in air, and thereafter applying 50 μl of water with four different concentrations of ethylene glycol (0, 10, 20 and 30 percent). After each spectra of left/right-scattered intensities had been achieved, the top substance was removed by highly absorbing papers and nitrogene gas and the next substance were introduced on top of the dimers.
The acquired data of the ratios of the left/right-scattered intensities in this experiment is illustrated in Figure 4.10 (a), which shows the ratio spectra for air plus five different concentrations of ethylene glycol in water with corresponding refractive index values in the legend. Figure 4.10 (b) shows the change in ratio versus refractive index for a constant wavelength of $\lambda = 664.5$ nm. Notice that no straylight subtraction have been performed during these measurements.

4.4.3 Performing local refractometric sensing in a microscope-free optical setup

Another essential property of a biosensing system is the ability to recognize small changes in the local dielectric environment, for instance when a certain amount of biomolecules binds to receptors on a Au surface [23]. The aim here is to get a significant change in left/right-scattering ratio signal in order to determine weather a certain amount of binding events have occurred.

To be able to distinguish if a certain type of molecule have attached the Au dimer disks their surfaces needs to be functionalized with receptors which allows this specific binding to occur.
In order to do real-time measurements we needed to register the signals from the left/right detectors simultaneously. Hence an additional optical system was built where the the fibers, containing the light from the left/right detectors, where mounted on top of each other parallely directed towards a lens system. The lenses focused the beams on to a CCD chip in a camera (Andor DV434-BV SH) with an optical filter (700 ± 20 nm) placed in front. The concept of local refractometric sensing performed during this experiment, and a sketch of the optical setup is illustrated in Figure 4.11.
The experiment was conducted by first placing 50 μl of water on top of the nanodimers and measure the ratio of left/right-scattered intensities over a time of approximately 1000 seconds. Thereafter 50 μl of a solution containing biotin-conjugated bovine serum albumin (bBSA), with a concentration of $C_b = 100$ $\mu g/ml$, was added and the ratio

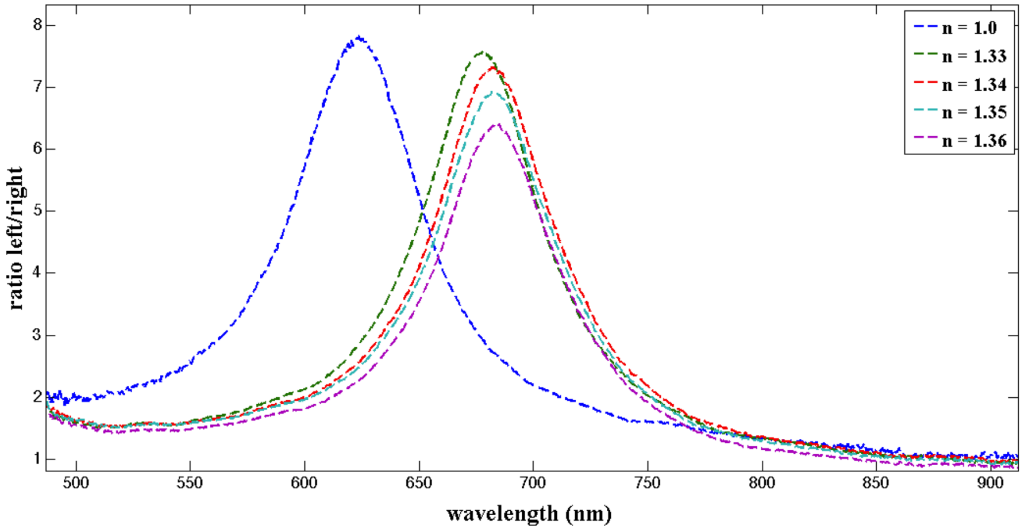

(a) *Illustration of how the ratio of left/right-scattered intensities changes when the refractive index of the upper medium is altered. The blue curve corresponds to the situation in air while the rest of the curves corresponds to different concentrations of ethylene glycol. Notice that no straylight subtraction have been performed during these measurements.*

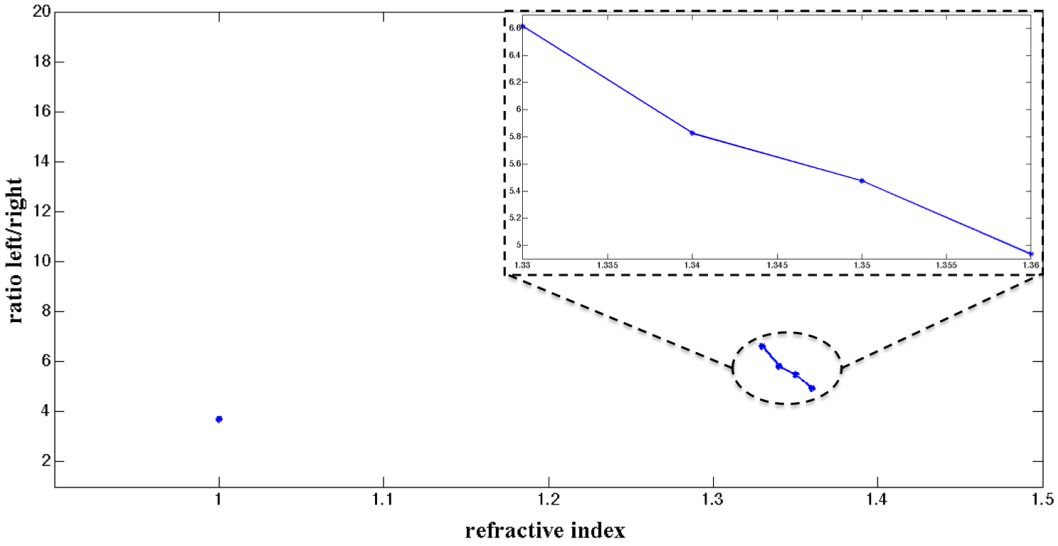

(b) *The change in ratio of left/right-scattered intensities when refractive index changes at a constant wavelength of 664.5 nm. Notice that the inset figure is a zoom-in which only illustrates the change in ratio for different concentrations of ethylene glycol.*

Figure 4.10: *Bulk refractive index sensing experiments performed in the microscope-free optical setup.*

was measured for another 1000 seconds. During this process bBSA will bind to the Au surfaces of the nanodisks causing a slight change in the refractive index of the local environment [24]. Finally 50 μl of a solution with a concentration of $C_n = 100$ $\mu g/ml$ neutravidin was added in order to study binding events with bBSA [25]. To study all possible binding events between neutravidin and bBSA a time interval of 2000 seconds was chosen.
Similar experiments have been conducted for LSPR shift refractometric detection where thoroughly washed samples was immersed in a solution consisting of 99 percent thiol-PEG and 1 percent thiol-PEG-biotin more than 24 hours. At the end of this process a sufficient amount of receptors will be attached to the dimer disk surfaces [26]. However to do a proof-of-principle study on this matter we skipped the thorough functionalization of the samples and used biotin-conjugated bBSA and neutravidin instead.

The data acquired in these measurements can be seen in Figure 4.12, where the time intervals corresponding to different stages are marked. After neutravidin was injected we can see the binding events as a continuous increase towards a saturated value in ratio of $R_I \approx 18.84$. Moreover we see that from the moment when the neutravidin solution was injected an increase in signal of $\Delta R_I \approx 0.76$ occurs. With a standard deviation of $\sigma_n = 0.0139$ for the saturated ratio value in this region we end up with a signal-to-noise value of $\Delta R_I/\sigma_n \approx 54.68$. The measurements was performed in a 0.15×150 seconds accumulation mode where each time frame corresponds to 30 seconds. This implies a 7.5 second read-out time for each frame.
The overall stability of the signals measured in the water-like environment can be viewed in Figure 4.13 which indicates that a significant noise reduction occurs when averaging over 100 time frames instead of studying a single one. When studying the noise levels in a single frame ($N = 1$) we get a standard deviation of $\sigma_1 = 0.085$, whereas when averaging over 100 frames ($N = 100$) we achieve $\sigma_{100} = 0.013$. From these values we see that $\sigma_{100} \approx \sigma_1/\sqrt{100}$ which means that we could expect a general decrease in standard deviation according to $\sigma_N \approx \sigma_1/\sqrt{N}$ when averaging over N time frames.

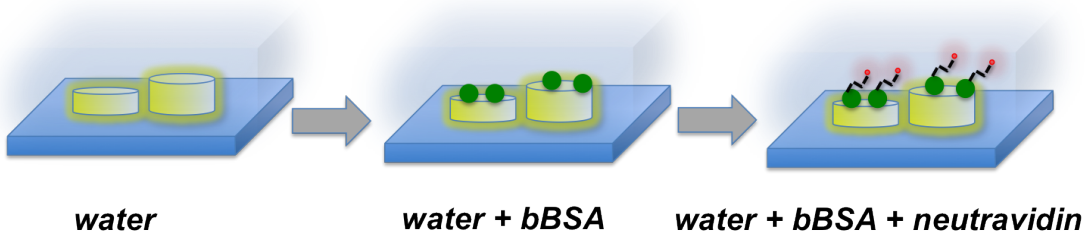

(a) *Illustration of the local refractometric sensing concept. The ratio of left/right-scattered signals are measured in real time over a certain time t. Afterwards bBSA and neatravidin are injected and the changes in ratio are studied over time.*

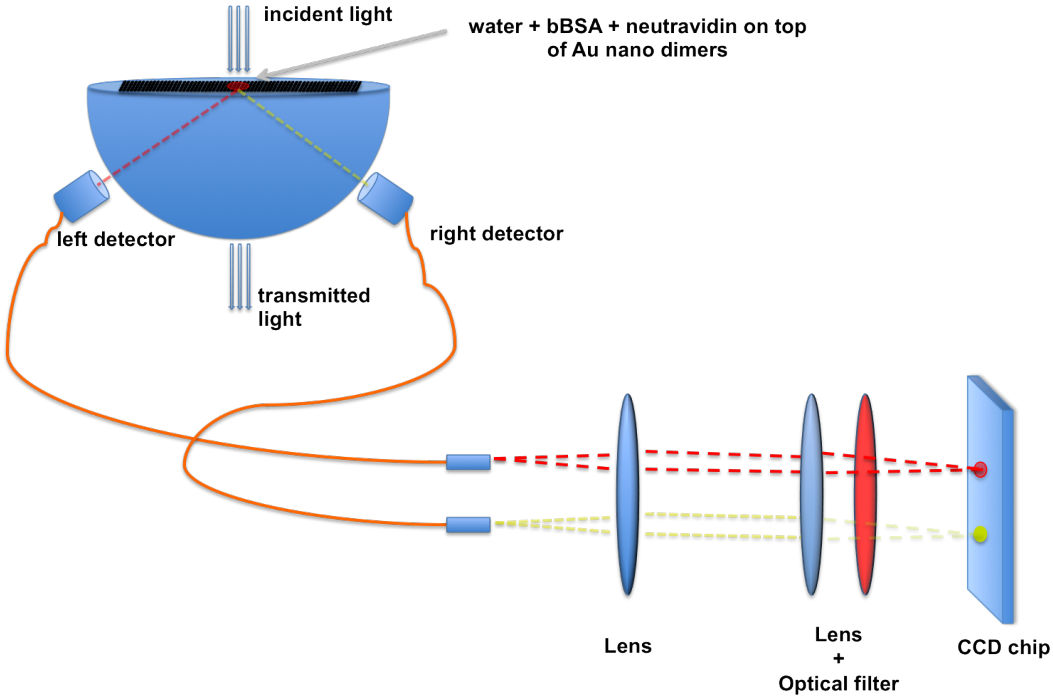

(b) *Illustration of the experimental setup which was used during the local refractometric measurements.*

Figure 4.11: *A schematic illustration of how the local refractometric sensing experiment was performed.*

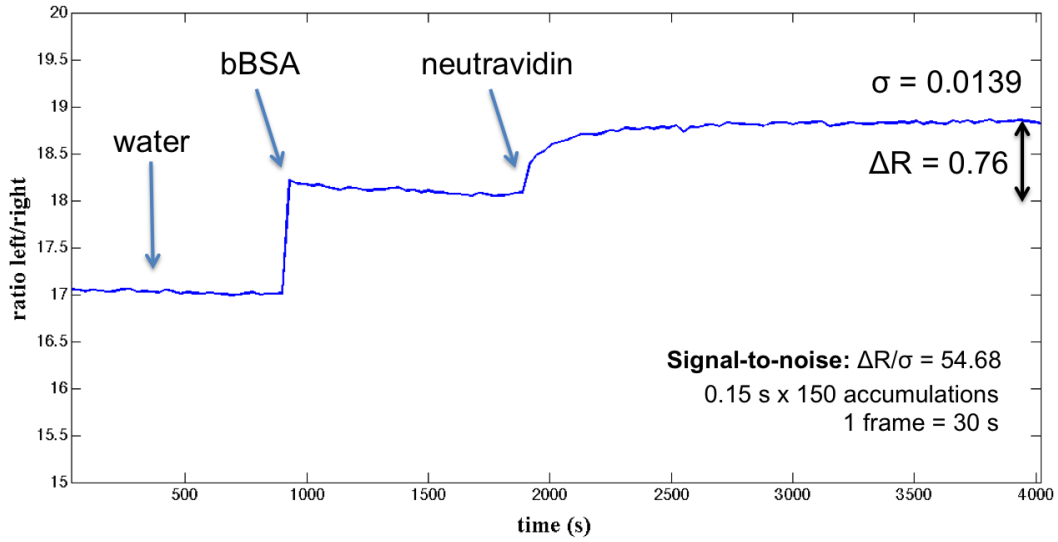

(a) *The data from the local refractometric sensing measurements.*

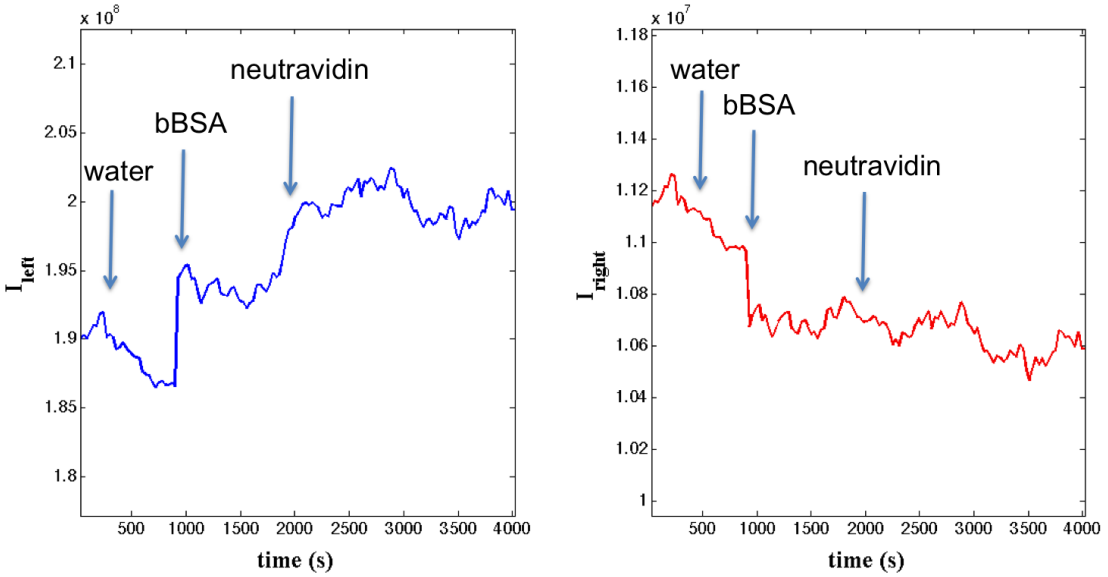

(b) *The acquired data from the left/right detector separately. From these figures it is not very clear if any binding events occur, whereas it is possible from the data acquired for the ratio. This is a strong indication that the self-referencing aspect of the optical system works.*

Figure 4.12: *Local refractive index sensing experiments performed in the microscope-free optical setup.*

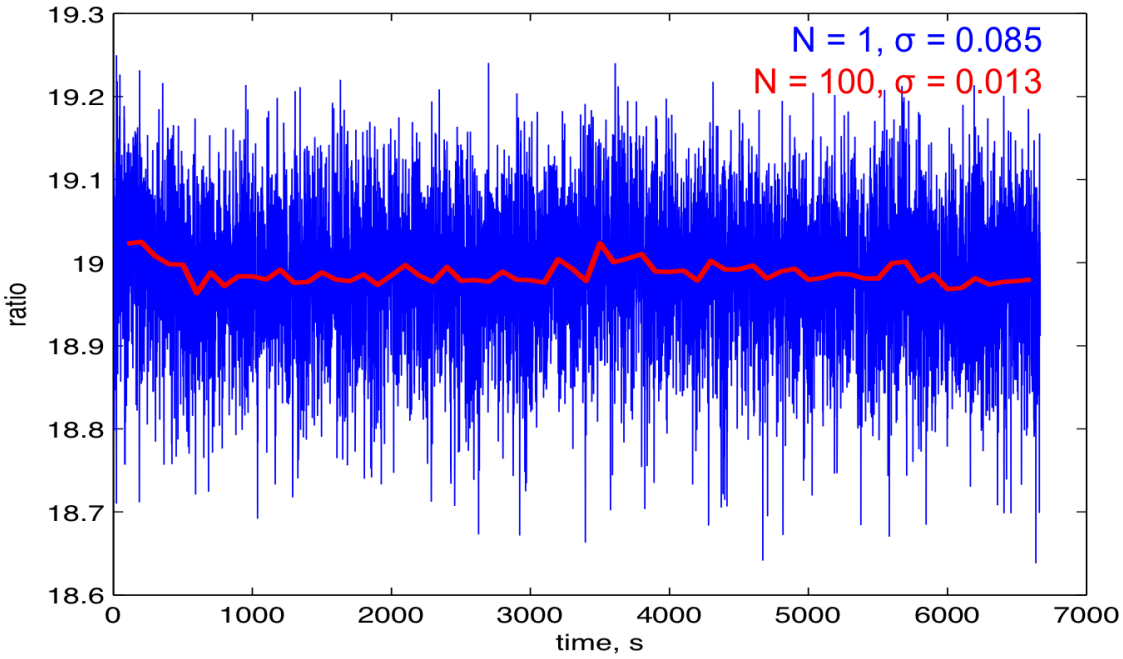

Figure 4.13: *An illustration of how noise levels can be decreased by averaging over 100 frames instead of studying a single one.*

5

Discussion/Conclusion

From the previously presented theoretical and experimental data there are many factors which supports comparable sensing ability for directional plasmonic nanodimers, compared with other sensing platforms such as detecting peak shift in extinction spectra. However the results also reveals several limiting factors for performing refractometric sensing such as noise levels and straylight. This section is dedicated to discussing the potentiality of monometallic nanodimer samples for refractometric sensing, supported by the heretofore presented both theoretical and experimental data.

To begin with, by studying and comparing Figures 4.6 (b), (d) and 4.10 (a), we see that they agree rather well on in which spectral region the directionality occurs. The data from both measurements indicates that the highest ratio of left/right-scattered intensities occur at $\lambda_a = 610 - 620$ nm for air and $\lambda_w = 670 - 690$ nm for water. The situation in air is moreover supported by the extinction spectrum for incident light polarized perpendicular with respect to the dimer axis, illustrated in Figure 4.3 (b).
From theoretical simulations, illustrated in section 2.7, the highest directional scattering effect will occur in the spectral region of the dip between the detuned resonance peaks, which is obviously the case when comparing Figure 4.3 (b) and Figure 4.6 (b). This is a strong indication that the theoretical estimations are correct in determining the spectral region where the directionality effect occurs. It also supports the argument that the microscope-free optical setup, described in Chapter 4.4, gives reliable measurements when detecting left/right-scattered intensities from the nanodimer samples.
By further investigating the image illustrated in Figure 4.8 (b) it is clear that the effect of directional scattering may be experienced by eye, without any spectrometer or microscope. It is clear that two different colours appears on the paper sheets in front of the left/right detectors. Hence by comparing this image with Figure 4.5 it is obvious that the hemispherical prism, in the microscope-free optical setup, projects a 2D

Fourier plane similar to that observed in the microscope (see Figure 4.4). One of the main beneficial aspects in the microscope-free setup, compared with the microscope, is that a larger portion of the transmitted light rays will be filtered out since the left/right detectors are positioned at an angle θ located in the forbidden zone. There are however still some possible contribution of straylight from both the glass substrate and the hemispherical glass prism since a comparison of scattering ratio magnitudes in Figures 4.10 and 4.6 (b). Obviously the straylight does not affect the spectral position of the directionality but it severely decreases the magnitude which may be problematic for the sensing aspect of the samples. However a ratio around 10 without straylight subtraction, supported by Figure 4.10, seems to be substantial for achieving sensing measurements [2].

The results from the bulk refractive index sensing measurements, illustrated in Figure 4.10 (b), supports that the sample have a directional scattering resonance sensitivity of $\xi_{DRS} \approx 79$ RIU^{-1} around $n \approx 1.33$ at a constant wavelength of $\lambda = 664.5$ nm. This result is extremely low in comparison with the sensitivity shown in Figure 3.1 (d). However by investigating the feature in Figure 4.10 (b), and comparing it with Figure 3.1 (d) we may draw the conclusion that the maximum value in ξ_{DRS} is tuned to a region of refractive indices in between the measured ones. Unfortunately it is hard to find suitable substances with refractive indices between $n = 1.0 - 1.33$, due to the fact that many of these substances are either non-liquids or damaging to the nanosamples [27]. This made it hard to do any experimental measurements to support the argument of a potential maximum in ξ_{DRS}.
However, by studying the time resolved scattering ratio measurements in Figure 4.13 we see that the signal appear to be relatively stable. With a standard deviation in water-like environments of $\sigma_w = 0.013$ and from $\xi_{DRS} = 79$ RIU^{-1} acquired by the bulk refractometric sensing measurements in Figure 4.10, we may estimate the ability in resolving changes Δn in refractive index by this specific sample. From the measured data we find that $\Delta n = \sigma_w / \xi_{DRS} \approx 1.64 \cdot 10^{-4}$ RIU which is relatively close to sensitivity reached by sensing schemes using detection of LSPR peak shift [26], though achieved here without any spectrometer.

It is clear that the manufactured samples together with the microscope-free optical setup indeed can perform local refractometric measurements which is an essential aspect for real biosensing. By studying the elapsing time from the moment when neutravidin was injected in Figure 4.12 (a), it is clear that we observe actual binding event between neutravidin and bBSA. The ratio signal continuously increases towards a saturated value around $R_I \approx 18.84$ at the end of the measurement. The feature of signal versus time in this case is relatively similar to what has been detected in previously LSPR measurements [26]. Since this project focuses on the proof-of-principle aspect of directional scattering resonance sensing, this result is of great importance.
Moreover the data acquired from the local refractometric sensing experiment in the microscope-free optical setup beautifully reveals the self-referencing aspect of the sensing scheme. By comparing Figure 4.12 (b) with Figure 4.12 (a), we see that it would not

be possible to observe any binding events by studying the left/right channel separately, whereas the ratio of the left/right-scattered intensities yields the three distinct phases water, water + bBSA and water + bBSA + neutravidin.

Even though the best sample, manufactured during the time period of the project, didn't support the supreme directional scattering features demonstrated by theoretical simulations in Figure 2.7, there are still many aspects which makes it worth continuing optimizing this sensing platform. One should have in mind that the theoretical models do not account for effects on directionality such as straylight originating from the glass substrate or shot noise caused by optical measuring devices [28]. Moreover the simulations are performed on an isolated monometallic Au dimer located on top of an infinitely wide and smooth plane glass interface. The radiation caused by each disk in the dimer was also approximated as originating from oscillating point dipole sources located in the center of the disks.
In reality there are in fact millions of dimer pairs with a certain distribution among their geometric parameters (see section 4.3), and since the directionality depends heavily on the aspect ratio of each dimer disk some dimer pairs will exhibit middling directional properties. Furthermore since the left/right-scattered light, registered by the detectors, consists of contributions from different dimer pairs with varying directional scattering abilities the ratio of the total detected intensities will have a less pronounced directionality feature. Due to the simplicity and low economic cost aspects in this study each nanosample was produced using the hole-mask colloidal lithography method (HCL) which will result in randomly distributed dimer pairs. This is avoided in fabrication methods such as *electron beam lithography (EBL)* but these methods are much more expensive and time consuming than HCL and was deliberately avoided [29].
The next section describes several different plausible ways to further increase the directionality features of the nanosamples .

5.1 Future work and optimization

There are several parameters in the earlier presented work which needs further improvement in order to achieve supreme sensitivities when conducting directional scattering ratio measurements.

First and foremost the samples, manufactured during the time period of this project, needs further optimization to reach a higher directionality. By studying the geometrical parameters, calculated from statistical measuring in software *ImageJ* from the SEM image (see Figure 4.2), we may conclude that the present geometries are not optimal.
For instance, the center-to-center distance $L = 114.01 \pm 7.93$ nm is rather far from fulfilling the condition $L = \lambda_{DRS}/4n \approx 154$ nm, where $\lambda_{DRS} \approx 615$ nm is the directional resonance scattering wavelength in air (see Figure 4.6 (b)). Since the constructive/destructive interference condition is highly dependent on the magnitudes of the dipoles $|\mathbf{p}_1|$ and $|\mathbf{p}_2|$, as well as the retardation/intrinsic phase difference $\pm kL - \Delta\varphi_{12}$,

we may assume that the ratio of left/right-scattered intensities can be much higher if the center-to-center distance L was larger. Hence, in the quest for suitable geometric dimensions there are still plenty of room for optimization.

Moreover we saw that the ratio of left/right-scattered intensities was severely decreased if the subtraction of straylight, originating from the glass substrate and the rest of the optical path, was ignored. By comparing the magnitudes of ratios in Figures 4.6 (b) and 4.10, we may estimate that the ratio is only 1/3 of the "true" value if straylight subtraction is avoided. Therefore this is yet another parameter to further optimize. For future development one could probably consider an optical setup with a shorter optical path in order to suppress the impact of straylight. The contribution of straylight to the left/right-scattered intensities are more rigorously described in Appendix A.1 at the end of this report.

Furthermore by investigating the base for the theoretical modulations in Chapter 2.7 we see that many realistic aspects are simplified and/or ignored. For instance the simulations are based on a single isolated dimer pair positioned on top of an infinitely wide and smooth glass substrate. Moreover the radiating dimer disks are approximated as oblate spheroids with a radiation originating from point dipole sources located in the center of each disk. To summarize, no straylight or other sources of noise and no dispersion of geometries between different dimer pairs are taken into account in this simulations. To approach a more realistic model one could investigate the electrodynamical picture which arises when applying the concept of Green's functions when simulating the interplay between plasmons and molecules [30]. In addition one could also try to simulate the noise from the surrounding environment to quantify the magnitude and spectral position of the directional scattering resonance.

By assuming that the signals contains shot-noise, we know that the standard deviation in each channel follows a Poisson distribution [31]. Therefore we will have $\sigma_L = \sqrt{I_L}$ and $\sigma_R = \sqrt{I_R}$ for the left/right channel respectively. Furthermore by assuming a constant ratio of $R = R_0 = I_L/I_R$ when measuring in a constant refractometric substance, we apply a propagation of errors σ_p to estimate the standard deviation of the ratio. This is done according to

$$\sigma_p = \sqrt{\sigma_L^2 \left(\frac{\partial R}{\partial I_L}\right)^2 + \sigma_R^2 \left(\frac{\partial R}{\partial I_R}\right)^2} = \frac{\sqrt{R_0(1+R_0)}}{\sqrt{I_R}} \approx \frac{R_0}{\sqrt{I_R}} \tag{5.1}$$

for $R_0 \gg 1$, so the relative noise is simply $\sigma_{rel} = \frac{\sigma_p}{R_0} \approx \frac{1}{\sqrt{I_R}}$. This yields that we need huge signals in order to get really low errors caused from shot-noise [32]. This result implies that to obtain signals with very low noise levels we either have to have an extremely strong light source or we have to collect signals over a very long time interval with a moderate power source. Anyhow, these are both factors which need further improvement and optimization.

Bibliography

[1] Shegai T., Svedendahl M., Chen S., Dahlin A., Käll M., *Nanoantennas for refractive-index sensing.* In: Agio M. & Alù A. *Optical antennas.* New York: Cambridge University Press; 2013. p. 340-356.

[2] Shegai T. *et al.*, *Directional scattering and hydrogen sensing by bimetallic Pd-Au nanoantennas.* NanoLetters. 2012; 2464-2469.

[3] Anker J. *et al.*, *Biosensing with plasmonic nanosensors.* Nature materials. 2008; Vol. 7.

[4] Novotny L. & Hecht B., *Principles of nano-optics.* New York: Cambridge University Press; 2006.

[5] Folland G. B., *Fourier analysis and its applications.* Providence: American Mathematical Society; 1992.

[6] Bohren C. & Huffman D., *Absorption and scattering of light by small particles.* New York: John Wiley & Sons; 1998.

[7] Becker J. *et al.*, *The optimal aspect ratio of gold nanorods for plasmonic bio-sensing.* Plasmonics, Vol. 5, pp. 161-167, 2010.

[8] Zhernovaya O. *et al.*, *The refractive index of human hemoglobin in the visible range.* Phys. Med. Biol. 56 (2011) 4013–4021.

[9] Evlyukhin A., *et al. Detuned electrical dipoles for plasmonic sensing.* NanoLetters. 2010; Vol. 10, 4571-4577.

[10] Okamoto T., *Near-field optics and surface plasmon polaritons.* Topics in Applied Physics, Springer 2001; Vol. 81, 97-122.

[11] Arfken G. B. & Weber H. J., *Mathematical methods for physicists (6th edition).* Burlington: Elsevier Academic Press; 2005.

[12] Miljković V. *et al.*, *Optical forces in plasmonic nanoparticle dimers.* J. Phys. Chem. C 2010, 114, 7472-7479.

[13] Meier V. & Wokaun A., *Enhanced fields on large metal particles: dynamic depolarization.* Optics Letters. 1983; Vol. 8; No. 11.

[14] Cheng D., *Field and wave electromagnetics: 2nd edition.* Boston: Addison-Wesley; 1989.

[15] Shegai T. *et al.*, *A bimetallic nanoantenna for directional colour routing.* Nature Communications. 2011.

[16] Hecht E., *Optics: 4th edition.* Boston: Addison-Wesley; 2001.

[17] Johnson P. & Christy R., *Optical constants of the noble metals.* Phys. Rev. B 6, 1972, 4370-4379.

[18] Hall D. B. *et al.*, *Spin coating of thin and ultrathin polymer films.* Polymer Engineering and Science, 1998, Vol. 38, No. 12.

[19] Fredriksson H. *et al.*, *Hole-mask colloidal lithography.* Advanced Materials. 2007; Vol. 19, 4297-4302.

[20] Rao A. *et al.*, *Characterization of nanoparticles using atomic force micrscopy.* Journal of Physics: Conference Series 61, (2007), 971–976.

[21] Tomar A. & Garg G., *Short review on application of gold nanoparticles.* Global Journal of Pharmacology 7 (1): 34-38, 2013.

[22] The MEGlobal Group of Companies. *Product guide: Ethylene glycol.* 2008; p. 25.

[23] John S. Mitchell & Yinqiu Wu (2010). *Surface plasmon resonance biosensors for highly sensitive detection of small biomolecules*, Biosensors, Pier Andrea Serra (Ed.), ISBN: 978-953-7619-99-2, InTech, DOI: 10.5772/7208.
Available from: http://www.intechopen.com/books/biosensors/surface-plasmon-resonance-biosensors-for-highly-sensitive-detection-of-small-biomolecules

[24] Chen H. *et al.*, *Enhancement of BSA binding on Au surfaces by calix(4)bisazacrown monolayer*, Sensors 2007, 7, 2263-2272.

[25] Orelma H. *et al.*, *Generic method for attaching biomolecules via avidin-biotin complexes immobilized on films of regenerated and nano brillar cellulose*, Biomacromolecules 2012, 13, 2802-2810.

[26] Chen S. *et al.*, *Ultrahigh sensitivity made simple: nanoplasmonic label-free biosensing with an extremely low limit-of-detection for bacterial and cancer diagnostics.* Nanotechnology 20 (2009), 434015 (9pp).

[27] The engineering toolbox: Refractive index of some common liquids (table) Available from: http://www.engineeringtoolbox.com/refractive-index-d1264.html

[28] Hobbs P. C. D., *Shot noise limited optical measurements at baseband with noisy lasers (proceedings Only)*, Proc. SPIE1376, Laser Noise, 216 (March 1, 1991).

[29] Rad M. & Ibrahim K., *Fabrication of nano-pit array using electron beam lithography.* Advanced Materials Research, Vol. 364 (2012). pp 169-173.

[30] Chen H. *et al.*, *Classical electrodynamics coupled to quantum mechanics for calculation of molecular optical properties: a RT-TDDFT/FDTD approach.* J. Phys. Chem. C 2010, 114, 14384–14392.

[31] Lund R. *et al.*, *Limiting properties of poisson shot noise processes.* J. Appl. Prob. 41, 911-918 (2004).

[32] Heath M. T., *Scientific computing: An introductory survey (2nd edition).* New York: McGraw-Hill; 2002.

A

Appendix

In this appendix a more detailed description of the impact of straylight to the ratio is reviewed. Moreover an alternative microscope-free optical setup is described which needs to be further improved in order to make reliable scattering measurements due to severe noise levels.

A.1 The impact of straylight on directional scattering ratios

It turns out that one of the major limiting factors for achieving supreme high directional scattering ratios is straylight originating from the glass substrate on which the nano dimers are located. Spectra showing the amount of straylight present in both air and water are illustrated in Figure A.1. From these figures one clearly see that the right scattered light is severly affected by the impact of the straylight. Since this data corresponds to the destructive interference light it is essential that the dip in the spectrum becomes very big in order to get high directional scattering ratios. By studying Figure A.1 (a) we can estimate that the amount of straylight compared with scattering is only 23% for left scattered intensity and 88% for right scattered intensity, in air at $\lambda = 615$ nm. From Figure A.1 (b) we get that the amount of straylight compared with left scattered light is 12% and 78% for right scattered light, in water at $\lambda = 678$ nm. This definitely supports that the effect of straylight subtraction is much higher for right scattered light than for left scattered light which results in a crucial increase in directional scattering ratio.
This is a true limiting factor for the sensing aspect since the ability to detect really small changes in the dielectric environment requires very high directional scattering ratios, this is demonstrated in Figure 3.1 (c) and (d).

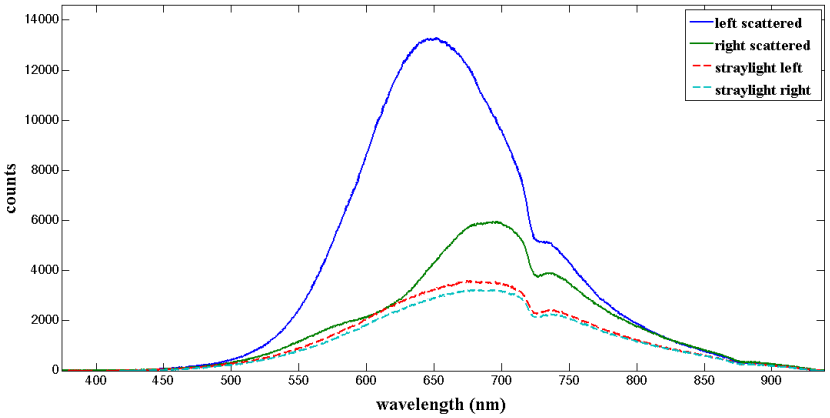

(a) *Figure showing the immense impact of straylight to the left/right-scattered intensities in air. It is obvious that performing a subtraction of the straylight spectra will result in a larger dip for the right-scattered light which will result in a higher directional scattering ratio.*

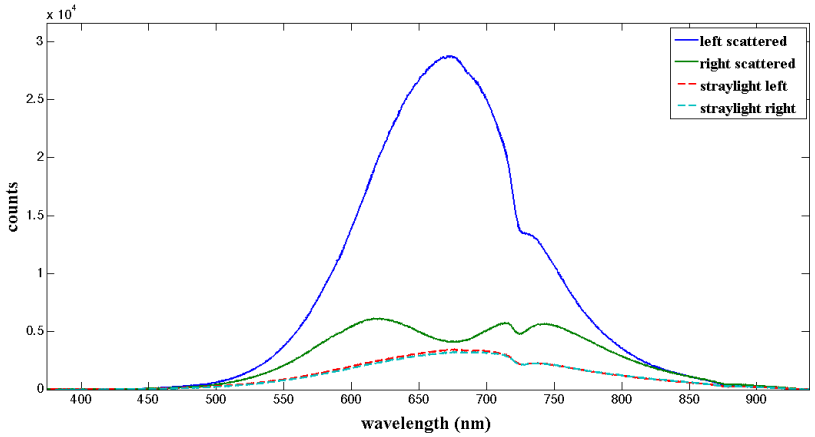

(b) *Figure showing the amount of straylight compared with scattered intensities when the dimers are located in water. By comparing with the figure above one clearly see that the straylight have a severe impact on the dip of the right-scattered spectrum.*

Figure A.1: *A comparison between the left/right-scattered intensities and the straylight spectra.*

A.2 An alternative microscope-free optical setup for directional scattering measurements

In this section an alternative microscope-free optical setup is considered in order to detect the left/right-scattered intensities originating from the radiating nanodimers.

The sample containing the nanodimers are put on top of a 3 mm thick glass slide and due to that the transformed wave will propagate in a direction at an angle $\theta_e \geq \theta_c$ with respect to the normal vector of the plane surface, it will hit the lower glass/air interface at an angle where the condition for total internal reflection is fulfilled. This behavior repeats it self and the wave will be trapped inside the glass disk until it reaches the surfaces where the detectors are placed. The schematic concept of the setup is illustrated in Figure A.2. The side surfaces of the glass disk is perpendicular to the totally

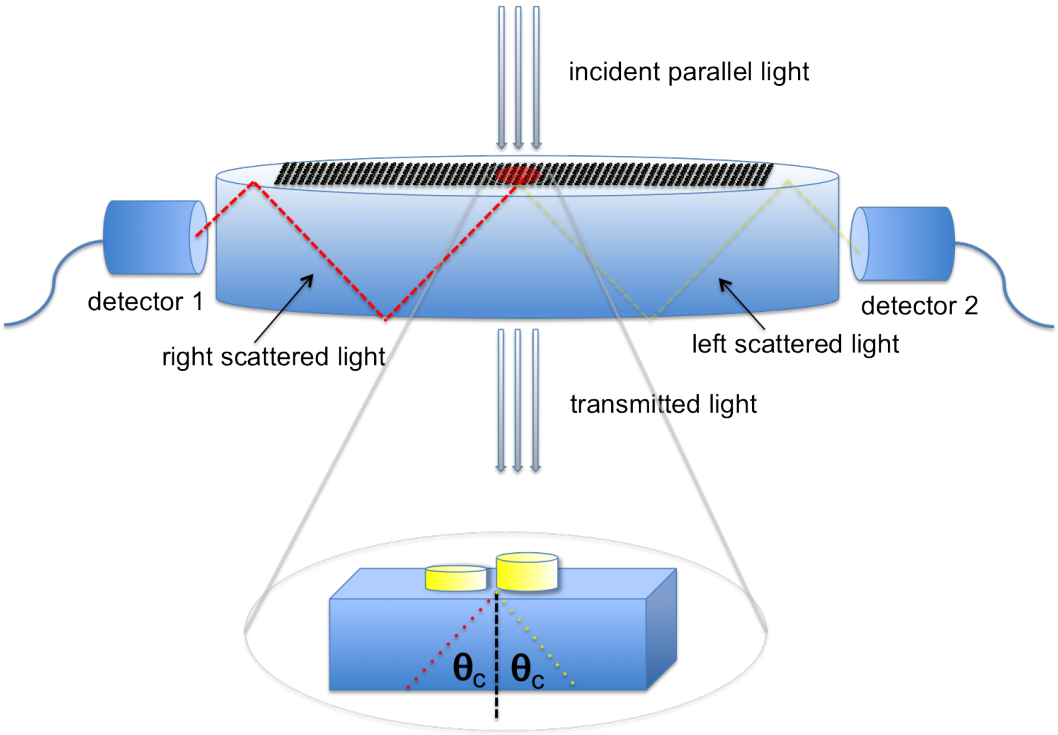

Figure A.2: *Schematic figure of the alternative microscope-free optical setup. The scattered light will be totally reflected until it reaches the detectors on the left/right side of he glass slide.*

reflecting surfaces and the wave will have an angle of incidence with respect to the sides denoted as θ_s. In order to detect as much light as possible we need to be sure that the majority of the scattered light doesn't totally reflect on the side surfaces of the disk, i.e. the condition $\theta_s < \theta_{c,air}$, where $\theta_{c,air}$ is the angle for total internal reflection for a glass/air interface should be fulfilled. If we denote the refractive indices of the nanopar-

ticle environment, the glass disk and the air as n_u, n_g and n_a respectively we know that $\theta_e = \arcsin(n_u/n_g)$ and $\theta_{c,air} = \arcsin(n_a/n_g)$. With this knowledge and the condition $\theta_s = 90^o - \theta_e < \theta_{c,air}$ to avoid total internal reflection on the sides of the glass disk, the condition $n_u \geq \sqrt{n_g^2 - n_a^2}$ need to be fulfilled.

When the nano dimers are located in air we will have $n_u = 1.0 < \sqrt{n_g^2 - n_a^2} \approx 1.12$ and some total reflection of the glass side surfaces will occur. But since light is scattered at larger angles than the critical in the forbidden zone we would expect to see some light transmitted through the side of the glass slide. However, since the majority of the experiments are aimed to be conducted with nanodimers in water like environments ($n_u \approx 1.33$) there will be no total internal reflection from the side surfaces.
This setup has yet another advantageous property compared with how detection measurements are usually carried out. The detectors are oriented parallel with the dimer axis and the incident light is polarized perpendicular to the dimer axis. Due to the theory of dipoles near planar interfaces, we know that light scattered by the plasmonic nanoparticles will concentrate in the forbidden zone mainly in a direction along the dimer axis. Furthermore since the incident light is sent from top creating a 90^o angle with the plane surface, the transmitted light will not be refracted by the glass disk (allowing efficient filtering of the scattered light). Moreover there will be no light scattered in to the forbidden zone from dipoles located far away from the surface which means that the scattered light from the radiating nanoparticles is the only radiation to survive all the way to the detectors.

This setup works reasonably well for determining the left/right-scattered intensities when considering symmetric dimers, as can be seen in Figure A.3 which shows a comparison between left/right-scattered intensities and previously measured extinction spectrum from a spectrometer. The spectra agree rather well with each other and the data obviously supports that no directionality is present for the symmetric monomer sample. However when measuring ratios of left/right-scattered intensities the setup does not deliver the desired results. The peak position for the directional scattering resonance coincide rather well with what is shown in Figures 4.6 and 4.10, but the magnitude is different. The most plausible reason for this has to do with straylight originating from scattering of the edges of the glass disk. Since the sides of the glass disk is relatively rough and unpolished a lot of the light hitting the side surfaces will bounce several times inside the disk, causing more straylight to the detected directional scattering signals. The left/right-scattered intensities and their corresponding ratios, measured in the alternative optic setup, can be seen in Figure A.4.
Even though the setup does not yield satisfactory properties at present it is still worth further development due to the immense simplicity that this system implies. In this setup no alignment is needed and no angular positioning of detectors is needed either.
Furthermore there are several plausible ways of decreasing the noise in the setup. For example, one can reduce the area located by the nanodimers to be of the same size as the spot size of the incident light. There is a possibility that when the scattered light is to-

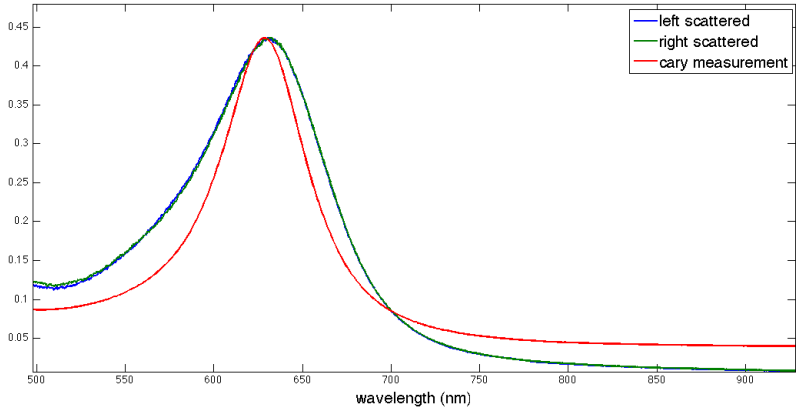

(a) *Figure showing a comparison between scattered intensities measured in the optical setup (blue and green curves), and previously measured extinction spectrum (red curve).*

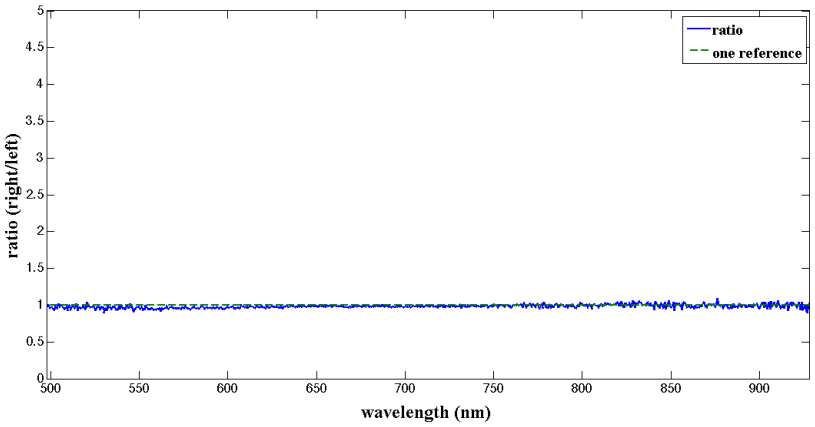

(b) *Figure showing the ratio of left/right-scattered intensities from the optical setup. Monomer samples yield no directionality which is supported by this data.*

Figure A.3: *A comparison between the left/right-scattered intensities measured in the optical setup and the extinction spectrum from measurements conducted in a spectrometer.*

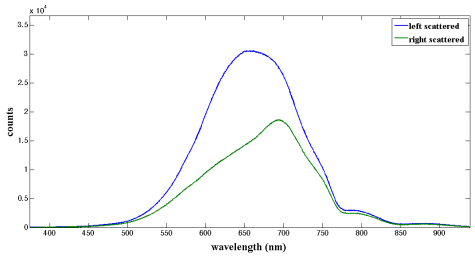

(a) *Figure showing the left/right-scattered intensities, measured in the alternative optical setup, when the nano dimers are located in air.*

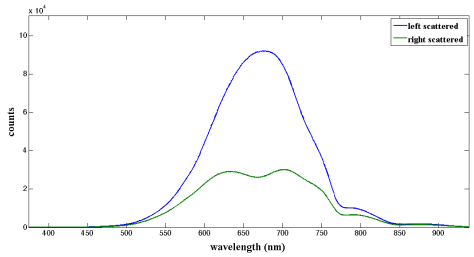

(b) *Figure showing the left/right-scattered intensities, measured in the alternative optical setup, when the nano dimers are located in water.*

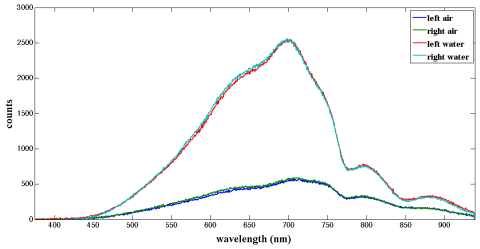

(c) *Figure showing the present straylight in both air and water.*

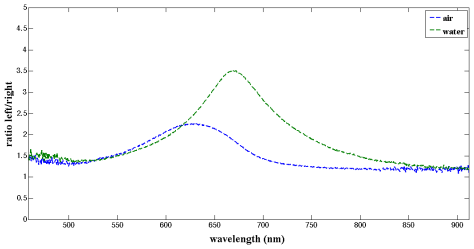

(d) *Figure showing the ratio of left/right-scattered intensities in air (blue curve) and water (green curve).*

Figure A.4: *Left/right-scattered intensity measurements conducted in the alternative optical setup.*

tally reflected within the glass disk it will further excite plasmons on the nanodisks when it hits the upper surface from underneath. By reducing the area of the substrate located by the nanodimers this effect will hopefully decrease and less noise will be present.